# Rapid Cortical Adaptation and the Role of Thalamic Synchrony During Wakefulness

**Nathaniel C. Wright[1], Peter Y. Borden[1], Yi Juin Liew[2], Michael F. Bolus[1], William M. Stoy[3], Craig R. Forest[3], Garrett B. Stanley[1]**

[1]Wallace H Coulter Department of Biomedical Engineering, Georgia Institute of Technology and Emory University, Atlanta, GA, USA

[2]Department of Biomedical Engineering, Georgia Institute of Technology, Emory University, Atlanta, GA, USA and Beijing University, Beijing China

[3] Department of Mechanical Engineering, Georgia Institute of Technology, Atlanta, Georgia, USA

**Abbreviated Title**: Cortical adaptation during wakefulness

**Pages/Figures:** 44 text pages, 8 Figures

**Word counts**: Abstract: 247, Introduction: 650, Discussion: 1494

**Correspondence:** Garrett B Stanley

Coulter Department of Biomedical Engineering
Georgia Institute of Technology & Emory University
313 Ferst Drive
Atlanta GA 30332-0535
USA

Phone: 404-385-5037
Fax: 404-385-5044
Email: garrett.stanley@bme.gatech.edu

**Conflict of Interest**: The authors declare no competing financial interests.

**Acknowledgements**: We thank Aurelie Pala, Audrey Sederberg, Adam Willats, Christian Waiblinger, and Elaida Dimwamwa for helpful comments on the data analysis and manuscript. We thank Aurelie Pala for assistance with spike-sorting, and Mahmood S. Hoseini for his assistance with the network model. **Funding**. This work was supported by NIH National Institute of Neurological Disorders and Stroke BRAIN Grant R01NS104928 (GBS), NIH National Institute of Mental Health BRAIN Grant U01MH106027 (GBS and CRF), NIH National Institute of Neurological Disorders and Stroke Pre-doctoral NRSA NS098691 (PYB), NIH National Eye Institute R01EY023173 (CRF), and National Science Foundation Graduate Research Fellowships (WMS, MFB).

***Abstract***

Rapid sensory adaptation is observed across all sensory systems, and strongly shapes sensory percepts in complex sensory environments. Yet despite its ubiquity and likely necessity for survival, the mechanistic basis is poorly understood. A wide range of studies primarily in in-vitro and anesthetized preparations have pointed to the emergence of adaptation effects at the level of primary sensory cortex, with only modest signatures in earlier stages of processing. The nature of rapid adaptation and how it shapes sensory representations during wakefulness, and thus the potential role in adaptive changes in perception, is unknown, as are the mechanisms that underlie this phenomenon. To address these unknowns, we recorded spiking activity in primary somatosensory cortex (S1) and the upstream ventral posteromedial (VPm) thalamic nucleus in the vibrissa pathway of the awake mouse, and quantified responses to whisker stimuli delivered in isolation and embedded in an adapting sensory background. We found that during wakefulness, cortical sensory responses were indeed adapted by persistent sensory stimulation; putative excitatory neurons were profoundly adapted, and inhibitory neurons only modestly so. Further optogenetic manipulation experiments and network modeling suggest this largely reflects adaptive changes in synchronous thalamic firing combined with robust engagement of feedforward inhibition, with little contribution from synaptic depression. Taken together, these results suggest that cortical adaptation results from changes in timing of thalamic input, and the way in which this differentially impacts cortical excitation and feedforward inhibition, pointing to a prominent role of thalamic gating in rapid adaptation of primary sensory cortex.

**Significance Statement**

Rapid adaptation of sensory activity strongly shapes representations of sensory inputs across all sensory pathways over the timescale of seconds, and has profound effects on sensory perception. Despite its ubiquity and theoretical role in the efficient encoding of complex sensory environments, the mechanistic basis is poorly understood, particularly during wakefulness. In this study in the vibrissa pathway of awake mice, we show that cortical representations of sensory inputs are strongly shaped by rapid adaptation, and that this is mediated primarily by adaptive gating of the thalamic inputs to primary sensory cortex and the differential way in which these inputs engage cortical sub-populations of neurons.

## *Introduction*

Our experience of the world around us depends upon context. For instance, a noisy environment provides persistent sensory stimulation, which can adapt the representations and percepts of salient sensory features embedded within the environment. Rapid sensory adaptation describes such interactions between stimulus history and perception, spanning milliseconds to seconds (Whitmire & Stanley, 2016). A wealth of human psychophysical studies have documented perceptual adaptation in audition (Bestelmeyer et al., 2010; Erb et al., 2013; Smith & Faulkner, 2006), vision (Anstis et al., 1998; C. Blakemore & Campbell, 1969; Colin Blakemore & Nachmias, 1971; Ghodrati et al., 2019), and somatosensation (Tannan et al., 2007), suggesting rapid sensory adaptation lends a vital flexibility to organisms tasked with surviving and thriving during rapid environmental changes.

Despite its ubiquity across sensory pathways and likely relevance to function (Barlow, 1961), the neural basis for rapid sensory adaptation is unknown. A large body of (mostly in vitro and anesthetized) work has implicated the early sensory pathway; adaptation effects cascade toward and culminate in primary sensory cortex (Ganmor et al., 2010; Lampl & Katz, 2017; Maravall et al., 2013), and the nature of the resulting cortical adaptation is consistent with well-documented perceptual effects. In the vibrissa pathway of the anesthetized rodent for example, adaptation induced through whisker stimulation shapes the amplitude (Boloori et al., 2010; Boloori & Stanley, 2006; Cohen-Kashi Malina et al., 2013; Ganmor et al., 2010; Heiss et al., 2008; Kheradpezhouh et al., 2017; Maravall et al., 2007; Ollerenshaw et al., 2014; Wang et al., 2010; Webber & Stanley, 2006, 2004) and spatial extent (Ollerenshaw et al., 2014; Zheng et al., 2015) of responses to subsequent stimuli in primary somatosensory cortex (S1). Yet two important questions remain unanswered. First, what is the nature of cortical response adaptation during wakefulness, where baseline activity is elevated relative to the anesthetized state (Aasebø et al., 2017; Greenberg et al., 2008; Vizuete et al., 2012)? It has been suggested that the thalamocortical pathway during wakefulness is in a baseline “adapted” state that is relatively impervious to additional adaptation (Castro-Alamancos, 2004), and the neural basis for perceptual adaptation lies elsewhere, but this has not been rigorously tested. Second, if the circuit is subject to sensory adaptation during wakefulness, what are the underlying mechanisms? Previous anesthetized and in-vitro work implicates thalamocortical and/or intracortical synaptic depression (Castro-Alamancos & Oldford, 2002; Chung et al., 2002; Cohen-Kashi Malina et al., 2013; Cruikshank et al., 2007, 2010; Gabernet et al., 2005), which could explain why mean evoked rates are generally more adapted in cortex than in thalamus (Chung et al., 2002; Gabernet et al., 2005; Khatri et al., 2004). Yet adaptation also reduces thalamic synchrony (Ollerenshaw et al., 2014; Wang et al., 2010) and single-unit bursting (Whitmire et al., 2016) under anesthesia.

Given the sensitivity of cortex to the timing of thalamic inputs (Bruno & Sakmann, 2006; Ollerenshaw et al., 2014; Swadlow & Gusev, 2001; Usrey et al., 2000; Wang et al., 2010), this suggests a potential role for thalamic spike timing in cortical adaptation.

Here, we address these unknowns by recording from and modeling S1 of the awake, head-fixed mouse during rapid sensory adaptation. We found that despite the relatively high level of baseline activity typical of the awake state, putative excitatory neurons in S1 were profoundly adapted by a background sensory stimulus. In particular, mean evoked firing rates, theoretical stimulus detectability, and synchronous cortical spiking were all significantly reduced in the adapted state, consistent with previously-reported decreases in detection performance. Several lines of evidence – including the recording of the thalamic inputs under a range of optogenetic controls and computational modeling – suggest this primarily reflected reduced synchronous thalamic firing and robust thalamically-driven feedforward inhibition in the adapted condition, with little contribution from thalamocortical and intracortical synaptic depression. Taken together, these results establish the role of the thalamocortical circuit in rapid adaptation during wakefulness, and implicate a more critical role of thalamic input than previously thought.

## ***Materials and Methods***

All procedures were approved by the Institutional Animal Care and Use Committee at the Georgia Institute of Technology (Protocol Numbers A100223 and A100225), and were in agreement with guidelines established by the National Institutes of Health.

### *Surgery*

Mice were induced with 5% isoflurane in an induction chamber, then transferred to a heating pad on a stereotaxic instrument, and maintained at 1 - 2% isoflurane for the remainder of the surgical procedure. A custom stainless steel headplate was fixed to the exposed skull with Metabond dental cement (Parkell, Inc.), exposed bone and tissue were then sealed with Metabond and super-glue (Loctite 404; Henkel). Metabond was used to fashion a well surrounding the left hemisphere. The well was filled with Kwik-Cast (World Precision Instruments, Inc.) and covered with a thin layer of Metabond, and the mouse was returned to its home cage. Mice were given pre- (buprenorphine) and post-operative (ketoprofen) analgesic, and were allowed to recover for three days before additional handling.

### *Habituation*

Three days after headplate implantation, mice were handled for at least 15 minutes, and then returned to their home cage. On subsequent days, mice were gradually habituated to head-fixation on a custom platform consisting of a tunnel with headpost clamps at one end. The first three daily habituation sessions lasted 15, 30, and 45 minutes respectively, but mice were returned to their home cage if they displayed signs of distress. We then gradually extended session durations until mice would tolerate at least 1.5 hours of fixation and whisker stimulation without signs of distress. Mice that did not meet these criteria were removed from the study, or used for anesthetized recordings (see below).

### *Awake electrophysiological recordings*

We recorded from five Ai32 x nsmf-cre, four C57BL/6J (wild-type) and one Ai32xPV-cre awake mice (up to three awake sessions per mouse). We used intrinsic optical signal imaging acquired under anesthesia to identify at least one putative principal column in S1. On the morning of the first recording session for each animal, we anesthetized the mouse as described above, and opened an approximately 500 micron x 500 micron craniotomy centered over a putative cortical column. When acquiring simultaneous VPm and S1 recordings, we opened a second craniotomy of similar size over the stereotactic

coordinates for VPm (1.8mm lateral from midline by 1.8mm caudal from bregma) and slowly inserted either a single-channel tungsten electrode (2 MOhm, FHC) or 32-channel silicon probe (NeuroNexus A1x32-Poly3-5mm-25s-177) to a depth of approximately 3 mm. We adjusted the depth while presenting continuous 10 Hz “sawtooth” stimulus trains to individual whiskers until we could identify a putative principal barreloid (by observing broad-waveform units with robust, short-latency, minimally-adapting sensory responses to stimulation of a single whisker, and at most comparatively weak responses to stimulation of surrounding whiskers (Brecht & Sakmann, 2002)), before slowly retracting the electrode/probe. We then covered exposed brain tissue with agarose, filled the well with Kwik-Cast, and allowed the mouse to recover in its home cage for at least two hours. After recovery, we head-fixed the awake mouse, removed the Kwik-Cast, filled the well with either saline, mineral oil, or agarose, and inserted an electrode/probe into each open craniotomy using a Luigs and Neumann manipulator. For S1 recordings, we inserted a multi-channel silicon probe (NeuroNexus) oriented 35 degrees from vertical. We used either a 32-channel linear (A1x32-5mm-25-177-A32), 32-channel “Poly3” (A1x32-Poly3-5mm-25s-177), or 64-channel, four-shank “Poly2” (A4x16-Poly2-5mm-23s-200-177) configuration probe. For VPm recordings, we inserted either a tungsten optoelectrode (2 Megaohm, FHC, with attached 200 micron optic fiber, Thorlabs), 32-channel silicon probe (A1x32-Poly3-5mm-25s-177) or 32-channel silicon optoelectrode (A1x32-Poly3-5mm-25s-177-OA32LP, with attached 105 micron optic fiber coupled to a 200 micron optic fiber, Thorlabs). Optic fibers were coupled to a 470 nm LED (M470F3, Thorlabs). When the barreloid we functionally identified during the anesthetized VPm mapping session was not topographically-aligned with the targeted S1 column, we referenced the (Coronal) Allen Brain Atlas to adjust the positioning of the VPm probe before descending. We inserted the probe(s) slowly to avoid excessive tissue dimpling, and waited at least 30 minutes after probe insertion to begin recording, to allow the tissue to settle. Continuous signals were acquired using a either a Cerebus (Blackrock Microsystems) or Tucker Davis Technologies acquisition system. Signals were amplified, filtered between 0.3 Hz and 7.5 kHz and digitized at either 30 kHz or 24414.0625 Hz.

After the first recording session, we removed the probe(s), covered exposed tissue with agarose, and sealed the well with Kwik-Cast and a thin layer of Metabond. We obtained either two or three recording sessions (one per day) from each mouse using the original craniotomy, but each time targeting a different cortical column and barreloid.

*Anesthetized extracellular recordings*

We recorded from three C57BL/6J (wild-type), four Ai32xPV-Cre, and three Ai32xnsmf mice under isoflurane anesthesia. Mice were anesthetized and implanted with headplates, and we opened a single craniotomy (either approximately 500 microns x 500

206 microns, or 1 mm x 1 mm) over S1, as described above. In some cases, the principal
207 column was first identified using intrinsic optical signal imaging, as described above. In
208 other cases, we inserted a single tungsten electrode into the stereotactic coordinates for
209 the center of S1, and defined the putative principal whisker to be that which evoked the
210 largest LFP response. We then inserted a 4 x 16 silicon probe array (A4x16-Poly2-5mm-
211 23s-200-177) to a depth of 700 microns. We oriented the probe to avoid blood vessels
212 on the cortical surface. For a subset of these experiments, we obtained additional
213 sessions by repeating the stimulation protocol using the whisker that evoked the
214 maximum LFP response on a shank different from the first. For each such session, we
215 determined the putative principal column off-line using white-noise-evoked spiking. For
216 each shank, we summed single- and multi-unit (see below) spiking across all trials for the
217 1 s window preceding feature onset. We divided the across-trial mean white-noise-
218 evoked response by the across-trial standard deviation of spontaneous spiking, and the
219 shank with the largest resulting value was determined to correspond to the principal
220 column.

221

222 *Anesthetized intracellular recordings*

223 We recorded ongoing, sensory-evoked, and light-evoked subthreshold activity from four
224 sensory- and light-responsive neurons in two mice using an Autopatcher system
225 (Kodandaramaiah et al., 2016), as described in detail previously (Stoy et al.,
226 2020). Briefly, we head-plated and identified the putative C2 column using intrinsic optical
227 signal imaging in two isoflurane-anesthetized Ai32xNR133 transgenic mice, and opened
228 a 1 mm x 1 mm craniotomy over the column, as described above. We then used an
229 Autopatcher 1500 (Neuromatic Devices) to provide pressure and measure pipette
230 resistance, and an algorithm based on these measurements to navigate around blood
231 vessels in an automated fashion while the pipette descended through cortical tissue.
232 Finally, we applied a recently-developed automated motion-compensation procedure
233 (Stoy et al., 2020) for synchronizing the motion of the pipette tip to that of the targeted
234 neuron prior to forming the seal. These experiments utilized Multiclamp 700B amplifiers
235 (Molecular Devices), and signals were digitized at 20 kHz (cDAQ-9174, National
236 Instruments), and recorded in PClamp 10 in current-clamp mode.

237

238 *Whisker stimulation*

239 We used a precise, computer-controlled galvanometer (Cambridge Technologies) with
240 attached tube to stimulate individual whiskers (Liew et al., 2020; Sederberg et al., 2019;
241 Waiblinger et al., 2018; Whitmire et al., 2016). The galvanometer was controlled using
242 either a custom Matlab GUI and Simulink Real-Time (Mathworks), or the Real-time

243 eXperiment Interface application (http://rtxi.org/), sampling at 1 kHz. We inserted the
244 whisker into the tube, which was positioned approximately 10 mm from the whisker
245 pad. We delivered "sawtooth" stimulus features (exponential rise and decay waveforms
246 lasting approximately 17 ms, with reported velocity defined by the average over the 8.5
247 ms rising phase (Wang et al., 2010)) either in isolation, or embedded in frozen sensory
248 white noise (i.e., white noise waveforms that were identical across trials). To generate
249 the white noise waveforms, the value at each time-step was drawn from a Gaussian
250 distribution (with standard deviation of one degree), and the resulting signal was lowpass-
251 filtered at 100 Hz (3rd-order Butterworth (Waiblinger et al., 2015)). The white noise
252 waveform around the feature waveform was dampened with an inverted Gaussian, with
253 standard deviation 25.5 ms.

254 The stimulus conditions were randomized across trials. The stimulus consisted of 1.5 s
255 of either white noise ("adapted" trials) or no white noise ("control" trials), with the onset of
256 the embedded feature at 1 s. The inter-trial interval was a random value (drawn from a
257 uniform distribution) between 2 and 3 s. We typically obtained at least 100 trials per
258 stimulus condition.

259

260 *Optogenetic stimulation*

261 In a subset of acute anesthetized experiments in Ai32xNR133 transgenic mice, we
262 stimulated thalamocortical terminals in S1 using blue (470 nm) light from an LED
263 (ThorLabs), and recorded either spiking or subthreshold S1 responses. We positioned
264 either a 200 or 400 micron optic fiber (ThorLabs) just above the exposed cortical surface,
265 adjacent to the probe or patch pipette. Light pulses were either 10 ms or 15 ms in
266 duration, and were delivered either in isolation or embedded in sensory white noise
267 delivered to the whisker by the galvanometer. We titrated the light level at the beginning
268 of each recording session to evoke cortical responses that were comparable in amplitude
269 to those evoked by punctate whisker stimulation.

270 In a subset of awake experiments in Ai32xNR133 transgenic mice, we presented the
271 above sensory stimulus protocol, in addition to a set of "LED" trials in which we delivered
272 a step input of 470 nm light to VPm beginning 1 s before and ending 0.5 s after the delivery
273 of an isolated sensory feature. The light was delivered via LED-coupled fiber attached to
274 the electrode/probe (described above). We titrated the light level at the beginning of each
275 recording session such that steady-state light-evoked firing rates in VPm (based on
276 threshold crossings of high-pass-filtered voltage recordings) approximately matched
277 those evoked by the white noise whisker stimulus.

278

279 *Spike-sorting*

We sorted spikes off-line using KiloSort2 (https://github.com/MouseLand/Kilosort2) for clustering, and phy (https://github.com/cortex-lab/phy) for manual curation of clusters. During manual curation, clusters were either merged or separated based primarily on waveform distributions across the probe and cross-correlogram structure. We discarded as "noise" those clusters whose across-instance mean waveform did not resemble a characteristic spike on any channel. All remaining clusters were labeled as either single- or multi-units by downstream analysis (see below).

*Units retained for analysis*

We labeled each curated cluster as either a single- or multi-unit based on the signal-to-noise ratio (SNR) and inter-spike interval (ISI) distribution. For each cluster and recorded spike, we calculated the absolute voltage difference between the trough and subsequent peak (VTP) on each channel. We defined the SNR to be the across-trial mean VTP divided by the across-trial standard deviation, for the channel on which the mean VTP was greatest. Additionally, we calculated "ISI violation percentage" for each cluster using the autocorrelogram (ACG). We defined the violation percentage to be the percentage of spikes in the 0 - 1 ms ACG bin. We then defined a well-isolated single-unit to be a cluster with SNR greater than 4.0, VTP greater than 50 mV, and ISI violation percentage below 1%. All other clusters were classified as multi-units. In our anesthetized recording sessions, we used an alternate probe configuration, which was somewhat less well-suited to obtaining well-isolated units. We therefore slightly relaxed our inter-spike interval violation constraints for defining "well-isolated" units, to yield more RS and FS cells from these datasets (see Methods). This did not qualitatively change our results. For S1, we further segregated single-units into regular- and fast-spiking units based on the mean waveform. Again using the channel on which the waveform was largest, we calculated the time from trough to subsequent peak (TTP). We classified S1 units as either fast-spiking (FS, putative inhibitory) or regular-spiking (RS, putative excitatory) neurons based on waveform width (Guo et al., 2017; Isett et al., 2018; McCormick et al., 1985; Niell & Stryker, 2010; Speed et al., 2019; Yu et al., 2019). Specifically, S1 units with TTP < 0.4 ms were classified as FS, and all others as RS. Waveforms were in general narrower for VPm units, consistent with previous work (Barthó et al., 2014). We therefore classified VPm "RS" cells as those with TTP > 0.3 ms, and excluded units with narrower waveforms, which likely originated from either the cell bodies or axon terminals of neurons in reticular thalamus (Barthó et al., 2014). For putative VPm units, we further required that the absolute peak of the PSTH of responses to isolated punctate stimuli occur between 2 and 10 ms of stimulus onset. Finally, when analyzing activity of single- and/or multi-units, we only included those units with at least 0.25 mean post-feature spikes per trial, and a significant change ($p < 0.05$, Wilcoxon signed-rank test) in firing rate after stimulus onset

on control (unadapted) trials, using the weakest sawtooth stimulus delivered during that recording session and 50 ms (30 ms) pre- and post-stimulus windows for S1 (VPm).

*Experimental Design and Statistical Analyses*

When comparing two sets of values (that were matched samples) across stimulus conditions, we used the Wilcoxon signed-rank test (implemented in Python using the wilcoxon function in the Scipy library), and Bonferroni-corrected resulting p-values for multiple comparisons where applicable. When comparing two independent samples (e.g., normalized response rates for RS and FS cells), we used the Kruskal-Wallis test (implemented in Python using the kruskal function in the Scipy library).

For any analysis resulting in a single value for a given recording session calculated using all trials (e.g., AUROC, mean synchronous spike rates, etc.), we tested for significance of change across conditions by re-sampling trials with replacement, re-calculating the final value for the re-sampled pseudo-data, and calculating the 95% confidence intervals (Bonferroni-corrected if necessary) of the resulting distribution of values.

The number of cells and animals used to calculate each reported result is included in the text of the Results section and/or figure captions.

*Analyses*

All analyses were performed using custom scripts in Python 3.0. The details of each analysis are presented below.

*ROC analysis*

We calculated the theoretical detectability of sensory features for each significantly-responsive RS unit (see above) by applying ideal observer analysis (Ollerenshaw et al., 2014; Wang et al., 2010) to the “population response” distributions for baseline and feature-evoked activity. For this analysis, we excluded putative inhibitory neurons (FS units), as we were interested in interpreting the loss of excitatory drive from cortical neurons, likely to play a role in downstream signaling and thus relevant for percepts. For each unit, we calculated the firing rate in a 50 ms baseline (pre-feature) and post-feature window on each trial. For baseline activity, we used a window beginning 500 ms preceding feature onset, as the white noise was largely dampened in the 50 ms window immediately preceding the feature on adapted trials. We then calculated the across-trial mean (μ) and standard deviation (σ) of the observed firing rates, and generated “population” firing rate distributions, or samples drawn from gamma distributions

parametrized by the data. Specifically, we drew 1000 samples from a gamma distribution $\Gamma(N * \alpha, \theta)$, where $\alpha = \mu^2/\sigma^2$, $\theta = \sigma^2/\mu$, and N is the assumed number of identical neurons to which the ideal observer has access (Britten et al., 1992; Stüttgen & Schwarz, 2008; Wang et al., 2010). We report results using N = 10, but results were qualitatively the same for N = 1, 5, and 20. For each feature velocity, we calculated the true- and false-positive rates for each threshold value between 0 and the maximum response amplitude, using steps of two standard deviations. We then generated the receiver operator characteristic (ROC) curves by plotting the set of true-positive values vs. the false-positive values. We quantified the theoretical detectability as the area under the ROC curve (AUROC). Because the sensory white noise was presented on adapted trials, it was possible that the adaptive decrease in feature detectability was due in some degree to elevated, white-noise-evoked baseline firing. To isolate the effects of feature response adaptation, we calculated AUROC for a "hybrid" condition using the feature-evoked distributions from adapted trials, and baseline distributions from control trials. Finally, we repeated this analysis by systematically varying the width of the baseline and feature-evoked windows, from 5 ms to 50 ms in 5 ms increments, yielding a time-resolved measure of feature detectability in each condition.

*Feature response latency and synchrony analysis*

We sought to estimate the feature response latency of each S1 unit from the PSTH. However, in contrast to the relatively well-populated grand PSTHs, the sparsely-populated PSTHs of individual neurons confound latency calculations. As such, we convolved the spike trains of each neuron with a Gaussian kernel (1 ms standard deviation), yielding a convolved aggregate spike count time series, or a smoothed PSTH. We defined the response latency ($T_{onset}$) for each stimulus condition to be the time at which the smoothed PSTH exceeded a threshold of four standard deviations of the pre-stimulus values (calculated from control trials). We further calculated the $T_{onset}$ adaptation index for each unit as the difference between adapted and control values divided by the sum of the values. Our reported results were qualitatively robust to reasonable choices of onset threshold (2.5, 3.5, 4.0, 5.0, and 6.0 standard deviations) and Gaussian kernel standard deviation (0.5, 1.0, 2.0, and 3.0 ms, not shown).

We calculated the population synchrony of feature responses for each recording session using the population grand cross-correlogram (CCG) of single- and multi-unit spiking. First, for each trial, unit, and spike, we calculated the relative time of all spikes from other simultaneously-recorded units in a +/- 20 ms window. We repeated this for all spikes, units, and trials, populating the grand CCG. We defined the population synchrony to be the proportion of spikes in the CCG in the +/- 7.5 ms window (Wang et al., 2010).

*Tonic and burst VPm spikes*

We classified spikes from well-isolated units in putative VPm as either burst or tonic based on criteria described previously (Whitmire et al., 2016). Bursts consisted of two or more sequential spikes from a single unit. We required at least 100 ms of quiescence before the first spike in the burst. Subsequent spikes were included in the burst if they occurred at most 4 ms after the previous spike. These criteria are consistent with the timing of burst spikes resulting from de-inactivation of T-type calcium channels after prolonged hyperpolarization.

*S1 membrane potential analysis*

We removed action potentials from intracellular voltage recordings by first identifying spike times and interpolating between the values 2.5 ms before and 2.5 ms after the peak of the action potential. To identify spike times in each recording, we first calculated the first time derivative time of the membrane potential at each time step. Spike onsets were defined to be positive crossings of five standard deviations of this time series. For each onset, the spike peak time corresponded to the next time at which the time derivative was less than or equal to zero. After interpolation, we low-pass-filtered the resulting time series (100 Hz, 3$^{rd}$ order Butterworth). For sawtooth sensory and optogenetic terminal stimulation responses, we calculated the across trial mean subthreshold response amplitude, time-to-peak, and width, using the same method as described above for the LFP.

*Thalamocortical network model*

We constructed a simple model of the thalamocortical network using custom scripts written in Python 3.6.10. All code is freely available upon request. We modeled a single cortical barrel as a clustered network of excitatory and inhibitory single-compartment leaky integrate-and-fire (LIF) neurons, subject to excitatory synaptic inputs from a “barreloid” of VPm neurons, and well as excitatory non-thalamic inputs that were independent across cortical neurons. For each of the “control” and “adapted” conditions, we simulated 50 trials, each lasting 150 ms, with a time-step of 0.05 ms.

We modeled a single VPm barreloid as forty independent trains of tonic and burst spikes, drawn from the empirical VPm PSTHs. The ongoing and evoked rates for each neuron were drawn from a skewed gamma distribution, to mimic the broad firing rate distributions of VPm neurons previously reported (Bruno & Simons, 2002; D. J. D. Pinto et al., 2000; Wang et al., 2010; Whitmire et al., 2016). Bursts were modeled as pairs of spikes with 2.5 ms ISI.

Non-zero thalamocortical (TC) synaptic weights were drawn from a broad distribution, to mimic the reported variability in TC synaptic strengths and/or efficacies (Bruno & Sakmann, 2006; Bruno & Simons, 2002; Cruikshank et al., 2007, 2010; Gabernet et al., 2005; Sermet et al., 2019). Mean initial TC synaptic strengths were the same for excitatory and inhibitory neurons (Sermet et al., 2019), but TC convergence was higher for inhibitory neurons (75% for inhibitory neurons, 50% for excitatory neurons), and VPm neurons with the highest firing rates did not synapse onto excitatory neurons (Bruno & Simons, 2002). In response to a spike in a given thalamic neuron, all TC synapses from that neuron instantly decayed (by a factor of 0.75), followed by exponential recovery (with time constant 25 ms).

We modeled a single cortical column as a network of 800 excitatory and 100 inhibitory LIF neurons, with relatively strong inhibitory-to-excitatory synapses (Gabernet et al., 2005). We imposed spatial clustering via “small-world” network connectivity (Bujan et al., 2015; Litwin-Kumar & Doiron, 2012; Wright, Hoseini, & Wessel, 2017; Wright, Hoseini, Yasar, et al., 2017), with 10% re-wiring probability. Inhibitory LIF neurons had shorter membrane time constants (Gentet et al., 2010) and refractory periods (1 ms for inhibitory, 2 ms for excitatory), which – together with the TC connection properties described above – supported higher firing rates in inhibitory neurons, as observed here during wakefulness (Fig. 1D – F) and in previous work (Bruno & Simons, 2002; Gentet et al., 2010; Khatri et al., 2004; Taub et al., 2013). Excitatory neurons were subject to an inhibitory spike-rate adaptation conductance, which helped to stabilize network activity.

We quantified model responses by calculating the peaks of the grand PSTHs for excitatory and inhibitory LIF neurons and divided “adapted” values by “control” values, yielding the normalized adapted response. We generated grand cross-correlograms (as described above) for 200 randomly-selected excitatory-excitatory and inhibitory-inhibitory pairs, and for 100 VPm-VPm pairs.

We further employed two alternate models to parse the roles played by synchronous thalamic spikes and feedforward inhibition. For the “reduced synch” model, we maintained the mean spike rates of the original model, but manually adjusted drawn VPm spike times to reduce synchrony. Specifically, if a drawn VPm spike time was within +/- 5 ms of the empirical PSTH peak time, we shifted the spike to a random later time, within approximately 20 ms of the PSTH peak. For the “Identical TC Connectivity” model, excitatory and inhibitory neurons had the same TC convergence values (50%), and we did not require that VPm neurons with the highest rates synapse exclusively onto inhibitory neurons.

462 ***Results***

463

464 To investigate the adaptive effects of persistent sensory stimulation on S1 sensory
465 responses during wakefulness, we presented precise deflections to a single whisker of
466 the awake, head-fixed mouse using a computer controlled galvanometer, and recorded
467 extracellular spiking activity in the corresponding principal column of S1, and/or principal
468 barreloid of VPm (Fig. 1A, see Methods). We presented punctate "sawtooth" sensory
469 features either in isolation or embedded in an adapting background stimulus (frozen
470 sensory white noise, Fig. 1A). The punctate stimulus feature captures the basic nature
471 of the high velocity "stick-slip" whisker motion events that occur as a result of whisker
472 contacts with larger surface irregularities during active sensation (Jadhav et al., 2009;
473 Jadhav & Feldman, 2010; Ritt et al., 2008; Wolfe et al., 2008). During whisker contacts
474 with surfaces, these stick-slip events are embedded in patterns of smaller-amplitude,
475 irregular deflections (Jadhav & Feldman, 2010), simplistically captured here utilizing low-
476 amplitude, repeatable background white noise whisker stimulation (Waiblinger et al.,
477 2015, 2018; Whitmire et al., 2016). We first characterized the effects of the background
478 stimulus on baseline and feature-evoked cortical firing during wakefulness (Figs. 1 – 3),
479 and then sought to identify the mechanisms underlying these effects through a battery of
480 additional experiments (Figs. 4 – 7) and thalamocortical network modeling (Fig. 8).

481

482 **S1 exhibits profound and differential sensory adaptation during wakefulness**

483

484 We first characterized the effects of the background white noise adapting stimulus on
485 baseline spiking activity in S1. We segregated well-isolated, sensory-responsive cortical
486 units into regular-spiking (RS, putative excitatory) and fast-spiking (FS, putative inhibitory)
487 neurons (Fig. 1B, see Methods). The sensory white noise evoked stimulus-locked spiking
488 in S1 (Fig. 1C) and significantly elevated mean rates relative to spontaneous activity (Fig.
489 1D). The effect was more pronounced for FS cells (Fig. 1C, D), consistent with previous
490 work demonstrating the higher sensitivity of S1 FS cells to relatively weak re-afferent
491 excitatory drive during whisking (Gutnisky et al., 2017; Yu et al., 2016, 2019).

492

493 Next, we investigated the adaptive effects of the background stimulus on the response to
494 sensory features during wakefulness. We delivered the 300 deg/s feature to a single
495 whisker, either in isolation (the "control" condition), or following 1 s of background
496 stimulation (the "adapted" condition, Fig. 1A, see Methods). To avoid distortion of the
497 feature waveform, the background stimulus was dampened with an inverted Gaussian
498 waveform in the neighborhood of the feature (Waiblinger et al., 2015; Whitmire et al.,
499 2016; see Methods). We delivered both moderate (300 deg/s) and relatively strong (900
500 deg/s) features in a subset of experiments. In the control condition, features
501 evoked robust, short-latency spiking responses, (Fig. 1E), consistent with previous work

502 in the anesthetized (Bruno & Simons, 2002; Khatri et al., 2004; D. J. Pinto et al., 2003;
503 Wang et al., 2010) and awake (Musall et al., 2014) rodent. We next asked whether the
504 background stimulus appreciably adapted feature responses, or whether the relatively
505 high baseline firing rates during wakefulness (Fig. 1D) resulted in a "pre-adapted" circuit
506 (Castro-Alamancos, 2004). We found that S1 feature responses were in fact substantially
507 muted when features were embedded in the background stimulus (Fig. 1E). To
508 characterize RS and FS feature responses and the effects of adaptation, we calculated
509 across-trial mean evoked rates using a 50 ms window following feature onset. For both
510 cell types and feature velocities, the peak (Fig. 1E) and mean (Fig. 1F) evoked rates were
511 reduced in the adapted condition. Interestingly, adaptation appeared to be more profound
512 for RS cells, in terms of proportional changes in sensory responses (Fig. 1E, F). To
513 further quantify the effects of adaptation on a cell-by-cell basis, and to capture cell-type-
514 specific adaptation, we calculated the normalized adapted response for each cell (i.e., the
515 across-trial mean adapted response rate divided by the mean control rate, see Methods).
516 For both feature velocities and cell types, population median normalized adapted
517 responses were less than one (capturing the general adaptive reduction in evoked rate),
518 and RS cells were indeed significantly more adapted than FS cells (Fig. 1G). This
519 differential effect was not specific to any cortical depth (Fig. 1H).
520
521 In summary, we observed profound rapid sensory adaptation in S1 of the awake mouse,
522 and cortical putative excitatory neurons were more adapted than putative inhibitory
523 neurons.
524
525 **Adaptation reduces the theoretical detectability of punctate sensory stimuli**
526
527 The adaptation of S1 feature responses should diminish the ability to distinguish the
528 sensory feature from the sensory background. To quantify the potential impact of
529 adaptation on feature detectability, we applied a signal detection theory framework to the
530 spiking activity of putative excitatory neurons, which are likely to play a role in downstream
531 signaling and thus are relevant for percepts. Qualitatively, theoretical feature detectability
532 is inversely related to the degree of overlap between the baseline and feature-evoked
533 firing rate distributions. For each S1 RS unit, we generated spike rate distributions using
534 50 ms windows of baseline and feature-evoked spiking, and drew samples from
535 "population" gamma distributions (Fig. 2A) parametrized by the empirical mean and
536 standard deviation ((Wang et al., 2010) see Methods). Consistent with the adaptive
537 decrease in single-neuron response rates, adaptation tended to move the feature-evoked
538 distribution toward the baseline distribution, increasing the degree of overlap (Fig. 2A,
539 right). We quantified the overlap by calculating the area under the receiver operator
540 characteristic curve (Wang et al., 2010; Whitmire et al., 2016) (AUROC, Fig. 2B), which
541 has a value of 1.0 for non-overlapping distributions, and 0.5 for complete

542 overlap. Adaptation significantly reduced the across-unit mean AUROC for both feature
543 velocities (by 19.1% for the 300 deg/s and 18.3% for the 900 deg/s feature, Fig. 2C,
544 bottom). Notably, repeating this analysis for a "hybrid" scenario using the adapted
545 feature-evoked distributions and control baseline distributions did not significantly alter
546 AUROC values relative to the true adapted condition (Fig. 2C, left), demonstrating that
547 the decrease in detectability reflected feature response adaptation, rather than an
548 elevation of baseline rates in response to the adapting stimulus.
549
550 The above analysis considers spiking in 50 ms pre- and post-feature windows, and the
551 results are consistent with the adaptation of mean feature-evoked RS rates. But it is also
552 apparent from visual inspection of the RS grand PSTHs that the time-course of S1 spiking
553 varied with feature velocity and sensory adaptation. To resolve the dependence of
554 feature detectability on time, we varied the width of the post-feature window from 5 ms to
555 50 ms in 5 ms increments (see Methods). Consistent with the RS grand PSTHs, we found
556 that in the control condition, AUROC values increased drastically in the first 15 ms of the
557 feature response, and reached peak values within 25 ms (Fig. 2C, right). The separation
558 between control and adapted AUROC values largely occurred during this early phase of
559 the response (Fig. 2C, right). In other words, the adaptive loss of theoretical detectability
560 largely reflected a decrease in short-latency feature-evoked spiking.
561
562 Together, these results quantify the degree to which sensory adaptation reduces the
563 theoretical detectability of sensory features during wakefulness, and demonstrate that this
564 largely reflects adaptation of the early feature response. This is qualitatively consistent
565 with previous reports showing significant adaptation of theoretical feature detectability in
566 the anesthetized rat (Ollerenshaw et al., 2014; Wang et al., 2010; Zheng et al., 2015),
567 and perceptual threshold in awake rats (Ollerenshaw et al., 2014; Waiblinger et al., 2015).
568
569 **Adaptation strongly influences the timing of feature-evoked spiking in S1**
570
571 As highlighted above, adaptation altered S1 sensory response timing, a key component
572 of cortical sensory representations that strongly influences how and what signals are
573 transmitted to downstream brain structures. Specifically, in addition to the dramatic
574 reduction in early feature-evoked spiking (particularly among RS cells), adaptation
575 caused an apparent increase in the latency of feature responses. These phenomena
576 may be relevant for interpreting the mechanistic basis of S1 adaptation, and the likely
577 perceptual implications; both are consistent with weaker feedforward excitatory drive to
578 S1, and could influence signaling to downstream targets. We therefore sought to quantify
579 these adaptive effects, and began by calculating the response latency ($T_{onset}$) for each S1
580 unit (see Methods). We found that for both RS and FS cells, and for both stimulus
581 strengths, adaptation increased $T_{onset}$ values (Fig. 3A). To further quantify and compare

582 adaptive changes in $T_{onset}$ across cell types, we calculated the $T_{onset}$ adaptation index (AI)
583 for each cell (see Methods) and compared population medians for RS and FS cells. For
584 both stimulus strengths, the adaptive increase in response onset times was significantly
585 greater for RS cells (300 deg/s RS median $T_{onset}$ AI = 0.21, FS median $T_{onset}$ AI = 0.02, p
586 = 1.21 x $10^{-4}$, Kruskal-Wallis test; 900 deg/s RS median $T_{onset}$ AI = 0.13, FS median $T_{onset}$
587 AI = 0.00, p = 4.93 x $10^{-4}$).
588
589 Next, we reasoned that the observed changes in S1 PSTH shapes might reflect a
590 decrease in synchronous spiking among cortical neurons. In general, the degree of
591 synchronous firing among a population of neurons is likely related to the effect on synaptic
592 targets; stronger inhibitory synchrony will tend to silence postsynaptic neurons, and
593 stronger excitatory synchrony will be more efficacious for driving postsynaptic neurons –
594 possibly downstream from S1. Indeed, it has been shown that coordinated population
595 firing is a better predictor than mean rates of stimulus identity (Jadhav et al., 2009; Safaai
596 et al., 2013; Zuo et al., 2015) and behavioral stimulus discrimination performance (Safaai
597 et al., 2013; Zuo et al., 2015) when rodents whisk across textured surfaces.
598
599 To calculate the prevalence of synchronous spikes in feature responses, we populated
600 the grand cross-correlogram (CCG) for RS-RS and FS-FS pairs for each stimulus
601 condition using spike trains from all pairs of simultaneously-recorded responsive cells,
602 and defined synchronous spikes to be those within a +/- 7.5 ms window around zero lag
603 (Fig. 3B, see Methods, Wang et al. 2010). We found that adaptation drastically reduced
604 the amplitude and sharpness of the RS-RS CCGs (Fig. 3C, left), while more modestly
605 reducing the grand CCG amplitude for FS-FS pairs (Fig. 3C, right). This represented a
606 significant decrease in synchronous spike counts for both pair types and stimulus
607 velocities (Fig. 3D, see Methods for definition of "valid pairs"). As reflected in the grand
608 CCGs, the decrease in FS-FS synchrony was significant, but proportionally smaller than
609 that of RS-RS synchrony.
610
611 Thus, rapid sensory adaptation in S1 during wakefulness not only reduced mean evoked
612 spike rates and theoretical feature detectability, but also disrupted timing through
613 increased response latencies and reduced synchrony. In both aspects of timing, as with
614 mean evoked rates, the adaptive effects on RS cells were more dramatic. The loss of
615 synchronous excitatory firing has implications for the driving of targets downstream of S1,
616 and ultimately for perception and behavior. The more modest decrease in synchronous
617 inhibitory firing implies that inhibitory neurons were still relatively strongly driven in the
618 adapted condition. Further, the synchronous inhibitory spiking that survives adaptation
619 should provide robust feedforward inhibition to S1 excitatory neurons, which may in part
620 explain the more profound adaptation of RS cells.
621

622 **S1 sensory responses are also adapted under anesthesia, but RS cells are not**
623 **differentially adapted**
624
625 Having established the extent and characteristics of rapid sensory adaptation in S1 of the
626 awake mouse, we next turned our attention to the underlying mechanisms. Our first step
627 in doing so was to compare these results to those from the anesthetized mouse, for two
628 reasons. First, while the background stimulus elevated S1 firing rates at least in part via
629 feedforward sensory inputs (as evidenced by the degree of stimulus-locked firing), it is
630 still possible that this adapting stimulus also evoked top-down modulation, e.g., through
631 systematic changes in ongoing S1 state via arousal-related neuromodulation (Mcginley
632 et al., 2015; McGinley et al., 2015; Reimer et al., 2014, 2016). In the anesthetized mouse,
633 ongoing state changes caused by endogenous processes should be independent of the
634 sensory white noise, and as such, white-noise-induced changes in mean feature
635 representations should not reflect top-down mechanisms. Second, isoflurane anesthesia
636 tends to silence the secondary posteromedial nucleus of thalamus (M. Suzuki & Larkum,
637 2020), lowers baseline cortical firing rates (Aasebø et al., 2017; Greenberg et al., 2008;
638 Vizuete et al., 2012), and generally weakens cortical inhibition (Haider et al., 2013) and
639 other intracortical interactions (M. Suzuki & Larkum, 2020). We therefore repeated our
640 experiments in a different set of mice lightly-anesthetized with isoflurane, using the
641 anesthesia to unmask the feedforward inputs from VPm to S1.
642
643 As expected, baseline firing rates under anesthesia were quite low compared to those
644 recorded during wakefulness (Fig. 4B, C). Despite these differences in baseline activity,
645 the anesthetized experiments recapitulated several key aspects of the awake data. First,
646 the background stimulus elevated baseline RS and FS firing rates (Fig. 4B, C), in the form
647 of stimulus-locked spikes (Fig. 4B). Further, adaptation clearly decreased the peak (Fig.
648 4D) and mean evoked firing rates of responses to 300 deg/s features (Fig. 4E), and
649 qualitatively shifted PSTHs to higher response latencies (Fig. 4D). Notably, however,
650 excitatory neurons were not differentially adapted under anesthesia (Fig. 4F). In light of
651 this, it is possible that the stronger cortical inhibition typical of wakefulness (Haider et al.,
652 2013) contributed to adaptation of RS cells in our awake recordings via robust
653 feedforward inhibition.
654
655 In summary, the elevation of (stimulus-locked) firing with presentation of background
656 sensory stimulation, and net adaptation of S1 feature responses was robust to
657 anesthesia, suggesting that feedforward mechanisms are sufficient to explain these
658 phenomena. In contrast, the differential adaptation of S1 excitatory neurons was
659 abolished by anesthesia, suggesting the set of mechanisms underlying this phenomenon
660 – possibly including strong feedforward inhibition – were not all active in the anesthetized
661 state.

662
663 **Adaptation primarily influences feature response timing in VPm thalamus**
664
665 Having established that several aspects of S1 sensory adaptation may reflect feedforward
666 mechanisms, we next sought to identify those mechanisms. Previous *in vitro* and
667 anesthetized work has demonstrated adaptation of evoked rate (Gabernet et al., 2005;
668 Ganmor et al., 2010; Hartings et al., 2003; Khatri et al., 2004; Liu et al., 2017; Ollerenshaw
669 et al., 2014; Wang et al., 2010; Whitmire et al., 2016), single-unit bursting (Whitmire et
670 al., 2016) and population synchrony (Ollerenshaw et al., 2014; Wang et al., 2010) in VPm,
671 suggesting S1 adaptation is inherited to some degree directly from VPm, yet this has
672 never been tested during wakefulness. We therefore next repeated our experiments
673 while recording spiking activity in VPm of the awake mouse (Fig. 5A, see Methods), and
674 asked how adaptation altered the rate and timing of thalamic sensory responses.
675
676 As in S1, we found that the background stimulus significantly elevated firing rates in VPm
677 (Fig. 5B, C) in the form of stimulus-locked spikes (Fig. 5B). We then characterized VPm
678 responses to sensory features, and the effects of the background stimulus on these
679 responses. We parsed VPm spikes into tonic and putative T-type calcium channel burst
680 spikes ((Whitmire et al., 2016), Fig. 5D, see Methods). We found that background
681 stimulation reduced feature-evoked tonic spiking (Fig. 5E, F), but this adaptive effect was
682 modest in comparison to the adaptation of S1 RS cells. Adaptation had a more striking
683 effect on burst firing and synchronous evoked spikes. Bursts – groups of spikes with very
684 short inter-spike intervals made possible by the de-inactivation of T-type calcium channels
685 (Kim et al., 2015; S. Suzuki & Rogawski, 1989) – have been shown to provide potent
686 synaptic drive to S1 (Sherman, 2001; Swadlow, 2002; Swadlow & Gusev, 2001), and may
687 therefore be critical for shaping cortical sensory responses. However, it is unknown
688 whether VPm bursting occurs during wakefulness, when VPm is likely to be on average
689 relatively depolarized, and T-type calcium channels inactivated. We did, in fact, observe
690 feature-evoked bursting, though burst spikes constituted a minority of total feature-evoked
691 spikes in the control condition (Fig. 5E). Adaptation profoundly reduced bursting, with
692 feature-evoked burst spikes nearly abolished in the adapted condition (Fig. 5E, F). We
693 further quantified synchronous thalamic firing by generating grand CCGs for each
694 stimulus condition, as done previously for S1 RS cells. In contrast to the modest
695 adaptation of evoked tonic spike rate, adaptation significantly and substantially decreased
696 synchronous VPm spike counts for both feature velocities (Fig. 5G, H).
697
698 In summary, rapid sensory adaptation modestly reduced feature-evoked tonic spiking in
699 VPm, and substantially reduced bursting and synchronous spiking. Given the sensitivity
700 of S1 to bursting and synchronous firing in VPm (Bruno & Sakmann, 2006; Ollerenshaw

et al., 2014; Sherman, 2001; Swadlow, 2002; Swadlow & Gusev, 2001; Usrey et al., 2000; Wang et al., 2010), this qualitatively predicts attenuated cortical responses.

**Thalamocortical synaptic depression contributes little to S1 sensory adaptation**

While the thalamic adaptation we observed likely played a key role in S1 adaptation, what was the additional contribution from thalamocortical and/or intracortical synaptic depression? Previous anesthetized work has demonstrated greater adaptation of mean evoked rates in S1 than in VPm (Chung et al., 2002; Gabernet et al., 2005; Khatri et al., 2004), and this has been interpreted to reflect thalamocortical synaptic depression. However, this may also reflect the sensitivity of cortex to bursting and synchronous thalamic firing, which we found to be profoundly adapted by persistent sensory stimulation. We sought to disentangle the relative contributions of thalamic response adaptation and thalamocortical and/or intracortical synaptic depression via two experiments in a transgenic mouse (Ai32xNsmf-Cre) expressing ChannelRhodopsin in VPm/VPl cell bodies, axons, and thalamocortical axon terminals.

In the first experiment, we presented an adapting background optogenetic stimulus that bypasses the early sensory pathway upstream of VPm, and measured the effects on S1 sensory feature responses. In this case, any observed S1 feature response adaptation should reflect thalamocortical and/or intracortical synaptic depression. We inserted an optoelectrode into VPm and a linear silicon probe into the topographically-aligned column of S1 of the awake mouse (Fig. 6A, see Methods). On “LED” trials, we elevated baseline VPm rates by substituting the adapting sensory stimulus with a step input of blue light to thalamus (Fig. 6B, right). We titrated the light power such that mean baseline thalamic rates were comparable to “white noise” trials (Fig. 6B, 6C, top). Interestingly, while the LED significantly increased VPm firing rates (Fig. B, C top, spont vs. LED), it did not significantly increase S1 firing rates (Fig. B, C, bottom), consistent with the notion that synchronous thalamic spikes are required to effectively drive cortical targets (Bruno & Sakmann, 2006).

We next inspected the effects of our manipulations on VPm and S1 sensory feature responses. We were interested in the presence or absence of gross adaptive effects, and so we grouped together tonic and burst spikes in VPm, and RS and FS cells in S1 for this analysis. On LED trials, we maintained a constant light level during presentation of the sensory feature, to avoid transient VPm responses to reduction in light power. As shown above, background sensory stimulation adapted feature responses in VPm and S1 (Fig. 6D). We next inspected the effects of optogenetically-elevated baseline VPm rates on feature responses. If the “artificial” elevation of baseline VPm rate adapted TC synapses prior to delivery of the sensory feature, we would anticipate adapted S1 feature

741 responses on LED trials, despite the non-adapted VPm feature response. On the
742 contrary, we observed no significant differences in S1 feature response rates between
743 the control and LED conditions (Fig. 6D, bottom), suggesting TC synaptic depression
744 contributed little to S1 feature response adaptation. Importantly, LED presentation did
745 not significantly enhance synchronous spike counts in the VPm feature response relative
746 to control trials (Fig. 6E), thus ruling out the possible confound of enhanced feature-
747 evoked thalamic synchrony masking the effects of synaptic depression.
748
749 As a further test of thalamocortical and intracortical synaptic strengths, we performed a
750 second set of experiments in which we presented the background sensory stimulus to
751 adapt the early sensory pathway, and a brief optogenetic feature stimulus that bypasses
752 the pathway upstream of the TC synapse. We positioned an LED-coupled optic fiber
753 above the cortical surface and recorded extracellular spiking activity with a silicon probe
754 array in S1 of the lightly-anesthetized mouse (Fig. 7A). On "sensory feature" trials, we
755 presented 300 deg/s sensory features, as described previously. On "light feature" trials,
756 we substituted the sensory feature with brief optogenetic stimulation of TC terminals in
757 the principal column, thus bypassing VPm cell bodies. In both cases, we presented the
758 features either in isolation (control trials) or embedded in a background sensory stimulus
759 (adapted trials). We then considered the responses of all S1 single- and multi-units that
760 responded significantly to both feature types (see Methods).
761
762 As shown above for awake and anesthetized mice, S1 sensory feature response grand
763 PSTHs exhibited profound sensory adaptation (Fig. 7B, left). If this largely reflected
764 synaptic depression, we would expect that light feature responses would be similarly
765 adapted by the background sensory stimulus. Instead, there was comparatively little
766 evidence of adaptation in the grand PSTHs for light feature responses (Fig. 7B, right).
767 This result also bore out in mean evoked rates: mean rates for sensory feature responses
768 were profoundly adapted (Fig. 7C, left), while light feature responses were only slightly
769 adapted (Fig. 7C, right), and the population median normalized adapted response was
770 near 1 for light feature responses, but significantly smaller for sensory feature responses
771 (Fig. 7D). Importantly, this did not simply reflect an overwhelmingly strong LED stimulus;
772 not only were evoked rates generally lower for the light feature than for the sensory
773 feature across all neurons (Fig. 7B, C), but in exploring a variety of LED stimulus
774 amplitudes and durations across experiments, we found that both relatively large- and
775 small-amplitude light-evoked responses were at most only modestly adapted (not shown).
776
777 We confirmed these observations of spiking activity by obtaining in vivo patch clamp
778 recordings from neurons in S1 of the lightly-anesthetized mouse (Fig. 7E, left, see
779 Methods). We recorded from four neurons that responded to both sensory and light
780 features. While sensory- and light-evoked amplitudes varied across neurons (Fig. 7F,

top), light feature responses were comparatively impervious to sensory adaptation. Specifically, for sensory feature responses, the across-trial mean amplitude significantly decreased for three cells, and the time to response peak significantly increased for all cells, (Fig. 7F, left, see Methods), consistent with the extracellular recordings (Fig. 7B, C). In contrast, light feature response amplitudes were unchanged and the time to peak response did not increase for any of these cells (Fig. 7F, right).

While there are important caveats to consider when interpreting responses to optogenetic terminal stimulation (see Discussion), when taken together with the profound effects of adaptation on synchronous VPm spiking and the lack of S1 adaptation under optogenetic elevation of baseline VPm rates, these results suggest that cortical feature response adaptation is primarily inherited from VPm, with thalamocortical and intracortical synaptic adaptation playing a lesser role.

**A model network identifies synchronous VPm spikes and robust feedforward inhibition as key mechanisms underlying S1 response adaptation**

We observed that S1 feature response rates were more profoundly adapted than VPm feature response rates, and we have proposed that this reflected the sensitivity of S1 to the adaptive loss of synchronous VPm spikes. Further, we hypothesized that feedforward cortical inhibition that was relatively robust to sensory adaptation helped to dampen feature-evoked S1 excitatory firing in the adapted condition. In other words, inhibition increased the sensitivity of cortical excitatory neurons to adaptation of synchronous VPm spiking. To test the reasonableness of these assertions, and to identify the mechanistic basis for robust feedforward inhibition, we implemented a model thalamocortical network, and assessed its ability to reproduce profound, cell-type-specific adaptation.

We modeled a single S1 barrel as a clustered network of 800 excitatory and 100 inhibitory leaky integrate-and-fire neurons, subject to excitatory inputs from a model “VPm barreloid” (Fig. 8A). The barreloid was modeled as 40 independent trains of tonic and burst spikes, with spike times drawn from the empirical VPm PSTHs. We selected cortical network and intrinsic neuronal parameters that mimicked measurements from previous studies, and then adjusted parameters slightly to ensure stable ongoing and evoked network activity (see Methods). Importantly, we implemented differential thalamocortical (TC) connectivity, which we hypothesized might explain the robustness of inhibitory firing to VPm adaptation. This differential connectivity consisted of three key components motivated by previous experimental work. First, inhibitory neurons had higher “TC convergence” (or proportion of VPm neurons that synapse onto each cortical neuron) than excitatory neurons (0.75 vs. 0.5, (Bruno & Simons, 2002)). Second, the baseline and evoked firing rate of each VPm neuron was drawn from a skewed distribution, and

821 VPm neurons with the highest rates synapsed exclusively onto inhibitory neurons ((Bruno
822 & Simons, 2002), see Methods). Finally, TC synaptic latencies were on average 1 ms
823 shorter for inhibitory neurons (Cruikshank et al., 2007; Kimura et al., 2010). With this
824 architecture in place, we modeled 50 trials from each stimulus condition of interest.

825 We fine-tuned the model parameters to give qualitatively realistic peak rates for excitatory
826 neurons when VPm spike times were drawn from the control (unadapted) empirical
827 PSTHs for the 300 deg/s and 900 deg/s sensory features (Fig. 8B). Thus, the excitatory
828 population was appropriately tuned to the rate and synchrony of thalamic firing. Next, we
829 repeated the simulations using VPm spikes drawn from the adapted PSTHs (Fig. 8B, top,
830 filled PSTH), and found that network excitatory neurons were in fact profoundly adapted,
831 despite the only modest reduction in mean VPm rates (Fig. 8B, center). Further, the
832 excitatory population was more strongly adapted than the inhibitory population (Fig. 8B,
833 C). Finally, as observed in experiment, synchronous spike counts were significantly
834 reduced in the adapted condition for excitatory-excitatory (Fig. 8D, left) and inhibitory-
835 inhibitory (Fig. 8D, right) pairs (see Methods), with a more drastic reduction for excitatory
836 neurons. Thus, the mechanisms incorporated in this simple model were sufficient to
837 qualitatively reproduce our key experimental results.

838 In these simulations, both the mean VPm rate (Fig. 8B, top) and VPm synchronous
839 spiking (Fig. 8E, top) were reduced in the adapted condition. We next assessed the
840 degree to which the loss in synchronous VPm spikes alone could explain cortical
841 adaptation. To do this, we repeated the simulations while "manually" manipulating VPm
842 spike times. Specifically, we first drew VPm spike times from the control PSTHs, and for
843 each spike that occurred within 5 ms of the PSTH peak time, we shifted the spike to a
844 random higher latency (within approximately 20 ms of the peak) with 30% probability (see
845 Methods). This had the effect of maintaining the mean evoked VPm rate, while reducing
846 the number of near-coincident pairs of VPm spikes in the early response (Fig. 8E, bottom,
847 "reduced synch" condition). We found that this change alone – which only modestly
848 affected the resulting VPm grand PSTH (Fig. 8F, top) – was sufficient to profoundly adapt
849 mean excitatory evoked rates (Fig. 8F, center; 8G, top) and synchronous spike counts
850 (Fig. 8H). In other words, with differential TC connectivity in place, a loss of synchronous
851 VPm spiking was sufficient to reproduce the adapted cortical network response.

852 Finally, we asked whether robust feedforward inhibition – mediated by differential TC
853 connectivity – contributed to the adaptation of network excitatory neurons. We modified
854 the network slightly by setting identical TC convergence and TC synaptic latency values
855 for excitatory and inhibitory neurons and eliminating rate-dependent TC connectivity (Fig.
856 8I). Inhibitory and excitatory neurons therefore had identical mean thalamocortical
857 connection properties, though differences in intrinsic neuronal properties and dense
858 excitatory-to-inhibitory connectivity still allowed for higher mean firing rates in the
859 inhibitory population (see Methods). We then slightly reduced the mean TC synaptic

weight to yield reasonable excitatory responses in the control condition (see Methods), before inspecting the responses to adapted VPm inputs. For this network, evoked rates (Fig. 8J, top, K) and synchronous spike counts (Fig. 8L, left) for excitatory neurons were only modestly adapted compared to the model with differential TC connectivity, and the degree of adaptation more closely matched that of the inhibitory population (Fig. 8K, L, right). In other words, the excitatory population was less sensitive to VPm adaptation when differential TC connectivity was removed. We used an additional set of models to further assess the relative importance of each component of the differential TC connectivity in the original model. While each component contributed, we found that the degree of excitatory adaptation was most sensitive to differences in TC synaptic latencies (not shown). This model thus demonstrates the role of robust feedforward inhibition – reflecting differential TC connectivity – in shaping the adaptation of cortical excitatory neurons.

Taken together, these modeling results support our hypotheses that the profound adaptation of cortical RS cells during wakefulness represents a loss of synchronous feature-evoked thalamic spikes, in conjunction with strong feedforward inhibition that is comparatively robust to this decrease in feedforward thalamic drive.

878 ***DISCUSSION***

879 To determine the nature of rapid sensory adaptation and how it shapes sensory
880 representations in primary sensory cortex during wakefulness, we recorded single-unit
881 activity in S1 of the awake, head-fixed mouse while presenting punctate sensory features
882 either in isolation, or embedded in a persistent background stimulus. To elucidate the
883 mechanistic basis of cortical adaptation, we identified putative excitatory and inhibitory
884 cortical neurons and recorded from the lemniscal inputs to S1, while employing a battery
885 of additional manipulations across the thalamocortical circuit. This approach allowed us
886 to infer the contributions from thalamic adaptation, thalamocortical synaptic depression,
887 and intracortical mechanisms. We further implemented a thalamocortical network model
888 constrained by these observations to explore the relative roles of various candidate
889 thalamic and cortical mechanisms.

890 Previous in vitro and anesthetized work has clearly demonstrated profound rapid sensory
891 adaptation in sensory cortex (Cohen-Kashi Malina et al., 2013; Ganmor et al., 2010; Heiss
892 et al., 2008; Kheradpezhouh et al., 2017; Lesica et al., 2007; Ollerenshaw et al., 2014;
893 Wang et al., 2010; Zheng et al., 2015), which is thought to represent the net effects on
894 the circuit of elevated firing rates. Yet because baseline cortical firing rates are elevated
895 during wakefulness compared to the anesthetized state (Aasebø et al., 2017; Greenberg
896 et al., 2008; Vizuete et al., 2012), it remains an open question whether any room is left
897 for fine-tuning by the sensory environment (Castro-Alamancos, 2004). Here, we
898 demonstrate that cortical sensory responses can indeed be profoundly adapted during
899 wakefulness. While we did not directly test the perceptual implications, the adaptive
900 decrease in theoretical feature detectability and synchronous firing of putative cortical
901 excitatory neurons suggest that downstream targets of S1 will be substantially less driven
902 in the adapted state, which in general predicts a decrease in perceived feature intensity
903 and a loss of detectability. In the specific context of the rodent whisker system, our
904 observations are consistent with previous behavioral work in rats, which demonstrated
905 changes in perceptual reporting following repetitive whisker stimulation (Ollerenshaw et
906 al., 2014; Waiblinger et al., 2015) and whisker self-motion (Ollerenshaw et al., 2012),
907 which elevates thalamic (Urbain et al., 2015) and cortical (Yu et al., 2016, 2019) firing
908 rates. In other words, this study supports previous in vitro and anesthetized work
909 suggesting cortical response adaptation could underlie adaptive changes in behavior.

910 We next sought to identify the mechanistic basis for S1 response adaptation. One body
911 of literature implicates thalamocortical synaptic depression (Castro-Alamancos & Oldford,
912 2002; Chung et al., 2002; Cruikshank et al., 2010; Gabernet et al., 2005), while our
913 previous work points to adaptation of thalamic spike timing (Ollerenshaw et al., 2014;
914 Wang et al., 2010; Whitmire et al., 2016), but both viewpoints have originated largely from
915 in vitro or anesthetized preparations. Our results here in the awake mouse support the
916 latter view. First, adaptation profoundly reduced single-unit bursting and the rate of

917 feature-evoked synchronous spikes in VPm, likely due to a combination of persistent VPm
918 depolarization (Whitmire et al., 2016) and adapted inputs from trigeminal (Castro-
919 Alamancos, 2002; Ganmor et al., 2010; Timofeeva & Lavalle, 2003) and reticular thalamic
920 (Ganmor et al., 2010; Hartings et al., 2003) neurons, which predicts attenuated cortical
921 firing (Bruno & Sakmann, 2006; Ollerenshaw et al., 2014; Swadlow & Gusev, 2001; Wang
922 et al., 2010). Further, optogenetic elevation of baseline VPm rates did not adapt S1
923 feature responses, and background sensory stimulation had little effect on S1 responses
924 to direct TC terminal stimulation. Finally, our modeling demonstrated that modest
925 reductions in synchronous VPm spiking predicted profound adaptation of downstream
926 excitatory neurons. Taken together, these results therefore demonstrate for the first time
927 in the awake animal the sensitivity of cortex to thalamic spike timing in the context of
928 sensory adaptation, and suggest that synaptic depression contributes little to the
929 observed S1 feature response attenuation.

930 This apparent lack of TC synaptic depression would seem to contradict the results of
931 previous anesthetized and in vitro studies (Castro-Alamancos & Oldford, 2002; Chung et
932 al., 2002; Cruikshank et al., 2010; Gabernet et al., 2005). We believe, however, that this
933 reflects a difference in the strength of adapting stimuli. Specifically, these previous
934 studies used adapting trains of high-velocity, punctate sensory stimuli and/or electrical
935 stimulation, whereas we employed a relatively low-amplitude white noise adapting
936 stimulus, which in terms of total power (Zheng et al., 2015) is many times weaker than
937 the adapting stimuli used in some previous studies (not shown). This almost certainly
938 adapts the TC circuit to a lesser degree than punctate stimulus trains, which may explain
939 the apparent contradiction with previous work. This likely also explains why we did not
940 observe stronger adaptation of FS units, which has been shown to reflect stronger
941 adaptation of TC synapses onto inhibitory neurons (Gabernet et al., 2005).

942 When interpreting the results of our optogenetic TC terminal stimulation experiments, it is
943 important to consider possible confounds. For example, light-evoked TC synaptic activity
944 may be unnaturally synchronous across synapses, which could potentially negate the
945 effects of synaptic depression. While we cannot rule out this possibility, we note that the
946 light feature evoked a broad range of firing rates across recording sessions (Fig. 7C), due
947 in part to our use of a variety of pulse amplitudes and durations, as well as variability in
948 responsiveness across animals. Yet even weak light-evoked S1 activity was not
949 appreciably adapted by sensory white noise, suggesting the results cannot be explained
950 by over-synchronization of TC synapses. The light may also have stimulated TC
951 terminals emanating from VPm neurons (in the principal and/or adjacent barreloids) that
952 were at most weakly responsive to sensory stimulation, meaning these synapses would
953 remain dormant (and unadapted) during background sensory stimulation. Still, this is
954 extremely unlikely to explain the nearly identical “control” and “adapted” LED responses
955 we observed; this would require that the LED primarily stimulated TC synapses from non-

956 responsive VPm neurons, with almost no contribution from the synapses of sensory-
957 responsive neurons in either the control or adapted conditions. This is unlikely, as we
958 only considered S1 units that were significantly responsive to both the sensory and light
959 features (and were therefore substantially innervated by sensory-responsive VPm
960 neurons).

961 While thalamic feature response adaptation appeared necessary for S1 adaptation, it did
962 not explain the differential adaptation of mean evoked rate, response latency, and evoked
963 synchronous spike counts among RS and FS cells during wakefulness. In other words,
964 RS and FS cells did not provide the same read-out of feature-evoked thalamic spiking.
965 In contrast, RS feature responses were no more adapted than FS rates under isoflurane
966 anesthesia, which has been shown to disproportionately weaken cortical inhibition
967 (Haider et al., 2013; Taub et al., 2013). This suggested to us that feedforward inhibition
968 contributed to the adaptation of RS cells during wakefulness. We explored this possibility
969 with a network model, in which we implemented cell-type-specific TC connectivity
970 motivated by previous experimental work (Bruno & Simons, 2002): cortical inhibitory
971 neurons were more densely innervated by TC synapses, and VPm neurons with the
972 highest rates synapsed exclusively onto inhibitory neurons, yielding a more excitable
973 inhibitory population. We found that S1 response adaptation did largely reflect a loss of
974 synchronous VPm spikes, but that the profound and differential adaptation of excitatory
975 neurons also required cell-type-specific TC connectivity. Taken together, these
976 experimental and modeling results suggest a thalamocortical circuit basis for the
977 observed S1 adaptation, involving a profound loss of synchronous feedforward excitation,
978 and only a modest decrease in dampening feedforward inhibition.

979 This adaptive shift in the feedforward E/I balance toward inhibition has implications for
980 cortical function and perception beyond attenuation of response amplitudes and
981 perceived stimulus intensities. For example, previous experimental work has
982 demonstrated that the relative strength and/or timing of cortical excitation and inhibition
983 contributes to the direction-selectivity (Wilent & Contreras, 2005) and receptive field
984 properties (Bruno & Simons, 2002; Kyriazi & Simons, 1993; Ramirez et al., 2014) of
985 excitatory neurons, maintains relatively low excitatory firing rates during bouts of whisking
986 (Gutnisky et al., 2017; Yu et al., 2016), shapes the “window of integration” during which
987 excitatory neurons integrate excitatory synaptic inputs and depolarize toward threshold
988 (Gabernet et al., 2005; Wilent & Contreras, 2005), and generally serves to “dampen”
989 thalamic-evoked spiking in the excitatory subnetwork (D. J. Pinto et al., 2003).
990 Thalamocortical adaptation exists on a continuum (Wang et al., 2010; Zheng et al., 2015),
991 and more moderate levels of adaptation than we imposed here may result in moderately
992 attenuated excitatory firing that is sharpened in space and time by comparatively non-
993 adapted inhibition, resulting in more faithful spatiotemporal cortical representations of
994 complex sensory stimuli. Future experiments exploring a broader range of adapting

stimulus strengths and using more complex single- and multi-whisker stimulation can explore these possibilities.

In summary, these results demonstrate the effects of rapid sensory adaptation on the early sensory pathway during wakefulness, culminating in profound adaptation of primary sensory cortex, while likely underlies perceptual adaptation on this timescale. Further, they highlight the relative importance of thalamic gating in establishing cortical adaptation, through population timing control of thalamic drive and the differential engagement of the inhibitory cortical sub-population.

## References


Aasebø, I. E. J., Lepperød, M. E., Stavrinou, M., Nøkkevangen, S., Einevoll, G., Hafting, T., & Fyhn, M. (2017). Temporal Processing in the Visual Cortex of the Awake and Anesthetized Rat. *Eneuro*, *4*(4), ENEURO.0059-17.2017. https://doi.org/10.1523/ENEURO.0059-17.2017

Anstis, S., Verstraten, F. A. J., & Mather, G. (1998). The motion aftereffect. *Trends in Cognitive Sciences*, *2*(3), 111–117. https://doi.org/10.1016/S1364-6613(98)01142-5

Barlow, H. B. (1961). Possible Principles Underlying the Transformations of Sensory Messages. In W. A. Rosenblith (Ed.), *Sensory Communication* (pp. 217–234). The MIT Press. https://doi.org/10.7551/mitpress/9780262518420.003.0013

Barthó, P., Slézia, A., Mátyás, F., Faradzs-Zade, L., Ulbert, I., Harris, K. D., & Acsády, L. (2014). Ongoing network state controls the length of sleep spindles via inhibitory activity. *Neuron*, *82*(6), 1367–1379. https://doi.org/10.1016/j.neuron.2014.04.046

Bestelmeyer, P. E. G., Rouger, J., DeBruine, L. M., & Belin, P. (2010). Auditory adaptation in vocal affect perception. *Cognition*, *117*(2), 217–223. https://doi.org/10.1016/j.cognition.2010.08.008

Blakemore, C., & Campbell, F. W. (1969). On the existence of neurones in the human visual system selectively sensitive to the orientation and size of retinal images. *The Journal of Physiology*, *203*(1), 237–260. https://doi.org/10.1113/jphysiol.1969.sp008862

Blakemore, Colin, & Nachmias, J. (1971). The orientation specificity of two visual after-effects. *The Journal of Physiology*, *213*(1), 157–174. https://doi.org/10.1113/jphysiol.1971.sp009374

Boloori, A.-R., Jenks, R. A., Desbordes, G., & Stanley, G. B. (2010). Encoding and Decoding Cortical Representations of Tactile Features in the Vibrissa System. *Journal of Neuroscience*, *30*(30), 9990–10005. https://doi.org/10.1523/JNEUROSCI.0807-10.2010

Boloori, A.-R., & Stanley, G. B. (2006). The Dynamics of Spatiotemporal Response Integration in the Somatosensory Cortex of the Vibrissa System. *Journal of Neuroscience*, *26*(14), 3767–3782. https://doi.org/10.1523/JNEUROSCI.4056-05.2006

Brecht, M., & Sakmann, B. (2002). Whisker maps of neuronal subclasses of the rat ventral posterior medial thalamus, identified by whole-cell voltage recording and morphological reconstruction. *The Journal of Physiology*, 495–515. https://doi.org/10.1013/jphysiol.2001.012334

Britten, K., Shadlen, M., Newsome, W., & Movshon, J. (1992). The analysis of visual motion: a comparison of neuronal and psychophysical performance. *The Journal of Neuroscience*, *12*(12), 4745–4765. https://doi.org/10.1523/JNEUROSCI.12-12-04745.1992

Bruno, R. M., & Sakmann, B. (2006). Cortex is driven by weak but synchronously active thalamocortical synapses. *Science (New York, N.Y.)*, *312*(5780), 1622–1627. https://doi.org/10.1126/science.1124593

Bruno, R. M., & Simons, D. J. (2002). Feedforward mechanisms of excitatory and inhibitory cortical receptive fields. *J Neurosci*, *22*(24), 10966–10975. https://doi.org/22/24/10966 [pii]

Bujan, A. F., Aertsen, A., Kumar, X. A., Kumar, A., & Kumar, X. A. (2015). Role of Input Correlations in Shaping the Variability and Noise Correlations of Evoked Activity in the Neocortex. *Journal of Neuroscience*, *35*(22), 8611–8625. https://doi.org/10.1523/JNEUROSCI.4536-14.2015

Castro-Alamancos, M. A. (2002). Properties of Primary Sensory (Lemniscal) Synapses in the Ventrobasal Thalamus and the Relay of High-Frequency Sensory Inputs. *Journal of Neurophysiology*, *87*(2), 946–953. https://doi.org/10.1152/jn.00426.2001

Castro-Alamancos, M. A. (2004). Absence of Rapid Sensory Adaptation in Neocortex during Information Processing States. *Neuron*, *41*(3), 455–464. https://doi.org/10.1016/S0896-6273(03)00853-5

Castro-Alamancos, M. A., & Oldford, E. (2002). Cortical sensory suppression during arousal is due to the activity-dependent depression of thalamocortical synapses. *The Journal of Physiology*, *541*(1), 319–331. https://doi.org/10.1113/jphysiol.2002.016857

Chung, S., Li, X., & Nelson, S. B. (2002). Short-term depression at thalamocortical synapses contributes to rapid adaptation of cortical sensory responses in vivo. *Neuron*, *34*(3), 437–446. https://doi.org/10.1016/S0896-6273(02)00659-1

Cohen-Kashi Malina, K., Jubran, M., Katz, Y., Lampl, I., Ebsch, C., & Rosenbaum, R. (2013). Imbalance between Excitation and Inhibition in the Somatosensory Cortex Produces Postadaptation Facilitation. *Journal of Neuroscience*, *33*(19), 8463–8471. https://doi.org/10.1523/JNEUROSCI.4845-12.2013

Cruikshank, S. J., Lewis, T. J., & Connors, B. W. (2007). Synaptic basis for intense thalamocortical activation of feedforward inhibitory cells in neocortex. *Nature Neuroscience*, *10*(4), 462–468. https://doi.org/10.1038/nn1861

Cruikshank, S. J., Urabe, H., Nurmikko, A. V., & Connors, B. W. (2010). Pathway-Specific Feedforward Circuits between Thalamus and Neocortex Revealed by Selective Optical Stimulation of Axons. *Neuron*, *65*(2), 230–245. https://doi.org/10.1016/j.neuron.2009.12.025

Erb, J., Henry, M. J., Eisner, F., & Obleser, J. (2013). The brain dynamics of rapid perceptual adaptation to adverse listening conditions. *Journal of Neuroscience*, *33*(26), 10688–10697. https://doi.org/10.1523/JNEUROSCI.4596-12.2013

Gabernet, L., Jadhav, S. P., Feldman, D. E., Carandini, M., & Scanziani, M. (2005). Somatosensory integration controlled by dynamic thalamocortical feed-forward inhibition. *Neuron*, *48*(2), 315–327. https://doi.org/10.1016/j.neuron.2005.09.022

Ganmor, E., Katz, Y., & Lampl, I. (2010). Intensity-Dependent Adaptation of Cortical and Thalamic Neurons Is Controlled by Brainstem Circuits of the Sensory Pathway. *Neuron*, *66*(2), 273–286. https://doi.org/10.1016/j.neuron.2010.03.032

Gentet, L. J., Avermann, M., Matyas, F., Staiger, J. F., & Petersen, C. C. H. H. (2010). Membrane potential dynamics of GABAergic neurons in the barrel cortex of behaving mice. *Neuron*, *65*(3), 422–435. https://doi.org/10.1016/j.neuron.2010.01.006

Ghodrati, M., Zavitz, E., Rosa, M. G. P., & Price, N. S. C. (2019). Contrast and luminance adaptation alter neuronal coding and perception of stimulus orientation. *Nature Communications*, *10*(1). https://doi.org/10.1038/s41467-019-08894-8

Greenberg, D. S., Houweling, A. R., & Kerr, J. N. D. (2008). Population imaging of ongoing neuronal activity in the visual cortex of awake rats. *Nature Neuroscience*, *11*(7), 749–751. https://doi.org/10.1038/nn.2140

Guo, W., Clause, A. R., Barth-Maron, A., & Polley, D. B. (2017). A Corticothalamic Circuit for Dynamic Switching between Feature Detection and Discrimination. *Neuron*, *95*(1), 180-194.e5. https://doi.org/10.1016/j.neuron.2017.05.019

Gutnisky, D. A., Yu, J., Hires, S. A., To, M. S., Bale, M. R., Svoboda, K., & Golomb, D. (2017). Mechanisms underlying a thalamocortical transformation during active tactile sensation. In *PLoS Computational Biology* (Vol. 13, Issue 6). https://doi.org/10.1371/journal.pcbi.1005576

Haider, B., Häusser, M., & Carandini, M. (2013). Inhibition dominates sensory responses in the awake cortex. *Nature*, *493*(7430), 97–102. https://doi.org/10.1038/nature11665

Hartings, J. A., Temereanca, S., & Simons, D. J. (2003). Processing of Periodic Whisker Deflections by Neurons in the Ventroposterior Medial and Thalamic Reticular Nuclei. *Journal of Neurophysiology*, *90*(5), 3087–3094. https://doi.org/10.1152/jn.00469.2003

Heiss, J. E., Katz, Y., Ganmor, E., & Lampl, I. (2008). Shift in the Balance between Excitation and Inhibition during Sensory Adaptation of S1 Neurons. *Journal of Neuroscience*, *28*(49), 13320–13330. https://doi.org/10.1523/JNEUROSCI.2646-08.2008

Isett, B. R., Feasel, S. H., Lane, M. A., & Feldman, D. E. (2018). Slip-Based Coding of Local Shape and Texture in Mouse S1. *Neuron*, *97*(2), 418-433.e5. https://doi.org/10.1016/j.neuron.2017.12.021

Jadhav, S. P., & Feldman, D. E. (2010). Texture coding in the whisker system. *Current Opinion in Neurobiology*, *20*(3), 313–318. https://doi.org/10.1016/j.conb.2010.02.014

Jadhav, S. P., Wolfe, J., & Feldman, D. E. (2009). *Sparse temporal coding of elementary tactile features during active whisker sensation*. *12*(6). https://doi.org/10.1038/nn.2328

Khatri, V., Hartings, J. A., & Simons, D. J. (2004). Adaptation in thalamic barreloid and cortical barrel neurons to periodic whisker deflections varying in frequency and velocity. *Journal of Neurophysiology*, *92*(6), 3244–3254. https://doi.org/10.1152/jn.00257.2004

Kheradpezhouh, E., Adibi, M., & Arabzadeh, E. (2017). Response dynamics of rat barrel cortex neurons to repeated sensory stimulation. *Scientific Reports*, *7*(1), 1–10. https://doi.org/10.1038/s41598-017-11477-6

Kim, H. R., Hong, S. Z., & Fiorillo, C. D. (2015). T-type calcium channels cause bursts of spikes in motor but not sensory thalamic neurons during mimicry of natural patterns of synaptic input. *Frontiers in Cellular Neuroscience*, *9*, 428. https://doi.org/10.3389/fncel.2015.00428

Kimura, F., Itami, C., Ikezoe, K., Tamura, H., Fujita, I., Yanagawa, Y., Obata, K., & Ohshima, M. (2010). Fast activation of feedforward inhibitory neurons from thalamic input and its relevance to the regulation of spike sequences in the barrel cortex. *Journal of Physiology*, *588*(15), 2769–2787. https://doi.org/10.1113/jphysiol.2010.188177

Kodandaramaiah, S. B., Holst, G. L., Wickersham, I. R., Singer, A. C., Franzesi, G. T., McKinnon, M. L., Forest, C. R., & Boyden, E. S. (2016). Assembly and operation of the autopatcher for automated intracellular neural recording in vivo. *Nature Protocols*, *11*(4), 634–654. https://doi.org/10.1038/nprot.2016.007

Kyriazi, H., & Simons, D. (1993). Thalamocortical response transformations in simulated whisker barrels. *The Journal of Neuroscience*, *13*(4), 1601–1615. https://doi.org/10.1523/JNEUROSCI.13-04-01601.1993

Lampl, I., & Katz, Y. (2017). Neuronal adaptation in the somatosensory system of rodents. *Neuroscience*, *343*, 66–76. https://doi.org/10.1016/j.neuroscience.2016.11.043

Lesica, N. A., Jin, J., Weng, C., Yeh, C.-I., Butts, D. A., Stanley, G. B., & Alonso, J.-M. (2007). Adaptation to Stimulus Contrast and Correlations during Natural Visual Stimulation. *Neuron*, *55*(3), 479–491. https://doi.org/10.1016/j.neuron.2007.07.013

Liew, J. Y., Pala, A., Whitmire, C. J., Stoy, W. M., Forest, C. R., & Stanley, G. B. (2020). Inferring Monosynaptic Connectivity Across Brain Structures In-Vivo. In *bioRxiv* (Vol. 106027). https://doi.org/https://doi.org/10.1101/2020.10.09.33393

Litwin-Kumar, A., & Doiron, B. (2012). Slow dynamics and high variability in balanced cortical networks with clustered connections. *Nature Neuroscience*, *15*(11), 1498–1505. https://doi.org/10.1038/nn.3220

Liu, C., Foffani, G., Scaglione, A., Aguilar, J., & Moxon, K. A. (2017). Adaptation of thalamic neurons provides information about the spatiotemporal context of stimulus history. *The Journal of Neuroscience*, 0637–17. https://doi.org/10.1523/JNEUROSCI.0637-17.2017

Maravall, M., Alenda, A., Bale, M. R., & Petersen, R. S. (2013). Transformation of

Adaptation and Gain Rescaling along the Whisker Sensory Pathway. *PLoS ONE*, *8*(12), e82418. https://doi.org/10.1371/journal.pone.0082418

Maravall, M., Petersen, R. S., Fairhall, A. L., Arabzadeh, E., & Diamond, M. E. (2007). Shifts in Coding Properties and Maintenance of Information Transmission during Adaptation in Barrel Cortex. *PLoS Biology*, *5*(2), e19. https://doi.org/10.1371/journal.pbio.0050019

McCormick, D. A., Connors, B. W., Lighthall, J. W., & Prince, D. A. (1985). Comparative electrophysiology of pyramidal and sparsely spiny stellate neurons of the neocortex. *Journal of Neurophysiology*, *54*(4), 782–806. https://doi.org/10.1152/jn.1985.54.4.782

McGinley, M. J., David, S. V., & McCormick, D. A. (2015). Cortical Membrane Potential Signature of Optimal States for Sensory Signal Detection. *Neuron*, *87*(1), 179–192. https://doi.org/10.1016/j.neuron.2015.05.038

Mcginley, M. J., Vinck, M., Reimer, J., Batista-Brito, R., Zagha, E., Cadwell, C. R., Tolias, A. S., Cardin, J. A., & Mccormick, D. A. (2015). Waking State: Rapid Variations Modulate Neural and Behavioral Responses. *Neuron*, *87*(6), 1143–1161. https://doi.org/10.1016/j.neuron.2015.09.012

Musall, S., Behrens, W. Von Der, Mayrhofer, J. M., Weber, B., Helmchen, F., Haiss, F., Von Der Behrens, W., Mayrhofer, J. M., Weber, B., Helmchen, F., Haiss, F., Behrens, W. Von Der, Mayrhofer, J. M., Weber, B., Helmchen, F., & Haiss, F. (2014). Tactile frequency discrimination is enhanced by circumventing neocortical adaptation. *Nature Neuroscience*, *17*(11), 1567–1573. https://doi.org/10.1038/nn.3821

Niell, C. M., & Stryker, M. P. (2010). Modulation of visual responses by behavioral state in mouse visual cortex. *Neuron*, *65*(4), 472–479. https://doi.org/10.1016/j.neuron.2010.01.033

Ollerenshaw, D. R., Bari, B. a, Millard, D. C., Orr, L. E., Wang, Q., & Stanley, G. B. (2012). Detection of tactile inputs in the rat vibrissa pathway. *Journal of Neurophysiology*, *108*(2), 479–490. https://doi.org/10.1152/jn.00004.2012

Ollerenshaw, D. R., Zheng, H. J. V., Millard, D. C., Wang, Q., & Stanley, G. B. (2014). The Adaptive Trade-Off between Detection and Discrimination in Cortical Representations and Behavior. *Neuron*, *81*(5), 1152–1164. https://doi.org/10.1016/j.neuron.2014.01.025

Pinto, D. J. D., Brumberg, J. C. J., & Simons, D. J. D. J. (2000). Circuit dynamics and coding strategies in rodent somatosensory cortex. *Journal of Neurophysiology*, *83*(3), 1158–1166. https://doi.org/10.1152/jn.2000.83.3.1158

Pinto, D. J., Hartings, J. A., Brumberg, J. C., & Simons, D. J. (2003). Cortical damping: Analysis of thalamocortical response transformations in rodent barrel cortex. *Cerebral Cortex*, *13*(1), 33–44. https://doi.org/10.1093/cercor/13.1.33

Ramirez, A., Pnevmatikakis, E. A., Merel, J., Paninski, L., Miller, K. D., & Bruno, R. M.

(2014). Spatiotemporal receptive fields of barrel cortex revealed by reverse correlation of synaptic input. *Nat Neurosci*, *17*(6), 866–875. https://doi.org/10.1038/nn.3720

Reimer, J., Froudarakis, E., Cadwell, C. R., Yatsenko, D., Denfield, G. H., & Tolias, A. S. (2014). Pupil Fluctuations Track Fast Switching of Cortical States during Quiet Wakefulness. *Neuron*, *84*(2), 355–362. https://doi.org/10.1016/j.neuron.2014.09.033

Reimer, J., Mcginley, M. J., Liu, Y., Rodenkirch, C., Wang, Q., McCormick, D. A., & Tolias, A. S. (2016). Pupil fluctuations track rapid changes in adrenergic and cholinergic activity in cortex. *Nature Communications*, *7*(May), 1–7. https://doi.org/10.1038/ncomms13289

Ritt, J. T., Andermann, M. L., & Moore, C. I. (2008). Embodied Information Processing: Vibrissa Mechanics and Texture Features Shape Micromotions in Actively Sensing Rats. *Neuron*, *57*(4), 599–613. https://doi.org/10.1016/j.neuron.2007.12.024

Safaai, H., von Heimendahl, M., Sorando, J. M., Diamond, M. E., & Maravall, M. (2013). Coordinated Population Activity Underlying Texture Discrimination in Rat Barrel Cortex. *Journal of Neuroscience*, *33*(13), 5843–5855. https://doi.org/10.1523/JNEUROSCI.3486-12.2013

Sederberg, A. J., Pala, A., Zheng, H. J. V., He, B. J., & Stanley, G. B. (2019). State-aware detection of sensory stimuli in the cortex of the awake mouse. *PLOS Computational Biology*, *15*(5), e1006716. https://doi.org/10.1371/journal.pcbi.1006716

Sermet, B. S., Truschow, P., Feyerabend, M., Mayrhofer, J. M., Oram, T. B., Yizhar, O., Staiger, J. F., & Petersen, C. C. H. (2019). Pathway-, layer-and cell-type-specific thalamic input to mouse barrel cortex. *ELife*, *8*, 1–28. https://doi.org/10.7554/eLife.52665

Sherman, S. M. (2001). A wake-up call from the thalamus. *Nature Neuroscience*, *4*(4), 344–346. https://doi.org/10.1038/85973

Smith, M. W., & Faulkner, A. (2006). Perceptual adaptation by normally hearing listeners to a simulated “hole” in hearing. *The Journal of the Acoustical Society of America*, *120*(6), 4019–4030. https://doi.org/10.1121/1.2359235

Speed, A., Del Rosario, J., Burgess, C. P., & Haider, B. (2019). Cortical State Fluctuations across Layers of V1 during Visual Spatial Perception. *Cell Reports*, *26*(11), 2868-2874.e3. https://doi.org/10.1016/j.celrep.2019.02.045

Stoy, W. M., Yang, B., Kight, A., Wright, N. C., Borden, P. Y., Stanley, G. B., & Forest, C. R. (2020). Compensation of physiological motion enables high-yield whole-cell recording in vivo. *Journal of Neuroscience Methods*, *November 2020*, 109008. https://doi.org/10.1016/j.jneumeth.2020.109008

Stüttgen, M. C., & Schwarz, C. (2008). Psychophysical and neurometric detection performance under stimulus uncertainty. *Nature Neuroscience*, *11*(9), 1091–1099.

https://doi.org/10.1038/nn.2162

Suzuki, M., & Larkum, M. E. (2020). General Anesthesia Decouples Cortical Pyramidal Neurons. *Cell*, *180*(4), 666-676.e13. https://doi.org/10.1016/j.cell.2020.01.024

Suzuki, S., & Rogawski, M. a. (1989). T-type calcium channels mediate the transition between tonic and phasic firing in thalamic neurons. *Proceedings of the National Academy of Sciences of the United States of America*, *86*(18), 7228–7232. https://doi.org/10.1073/pnas.86.18.7228

Swadlow, H. A. (2002). Thalamocortical control of feed-forward inhibition in awake somatosensory “barrel” cortex. *Philosophical Transactions of the Royal Society B: Biological Sciences*, *357*(1428), 1717–1727. https://doi.org/10.1098/rstb.2002.1156

Swadlow, H. A., & Gusev, A. G. (2001). The impact of “bursting” thalamic impulses at a neocortical synapse. *Nature Neuroscience*, *4*(4), 402–408. https://doi.org/10.1038/86054

Tannan, V., Simons, S., Dennis, R. G., & Tommerdahl, M. (2007). Effects of adaptation on the capacity to differentiate simultaneously delivered dual-site vibrotactile stimuli. *Brain Research*, *1186*(1), 164–170. https://doi.org/10.1016/j.brainres.2007.10.024

Taub, A. H., Katz, Y., & Lampl, I. (2013). Cortical Balance of Excitation and Inhibition Is Regulated by the Rate of Synaptic Activity. *Journal of Neuroscience*, *33*(36), 14359–14368. https://doi.org/10.1523/JNEUROSCI.1748-13.2013

Timofeeva, E., & Lavalle, P. (2003). The Relay of High-Frequency Sensory Signals in the Whisker-to-Barreloid Pathway. *The Journal of Neuroscience*, *23*(17), 6778–6787. https://doi.org/10.1523/JNEUROSCI.23-17-06778.2003

Urbain, N., Salin, P. A., Libourel, P. A., Comte, J. C., Gentet, L. J., & Petersen, C. C. H. (2015). Whisking-Related Changes in Neuronal Firing and Membrane Potential Dynamics in the Somatosensory Thalamus of Awake Mice. *Cell Reports*, *13*(4), 647–656. https://doi.org/10.1016/j.celrep.2015.09.029

Usrey, W. M., Alonso, J.-M., & Reid, R. C. (2000). Synaptic Interactions between Thalamic Inputs to Simple Cells in Cat Visual Cortex. *The Journal of Neuroscience*, *20*(14), 5461–5467. https://doi.org/10.1523/JNEUROSCI.20-14-05461.2000

Vizuete, J. A., Pillay, S., Diba, K., Ropella, K. M., & Hudetz, A. G. (2012). Monosynaptic functional connectivity in cerebral cortex during wakefulness and under graded levels of anesthesia. *Frontiers in Integrative Neuroscience*, *6*(SEPTEMBER), 1–11. https://doi.org/10.3389/fnint.2012.00090

Waiblinger, C., Brugger, D., Whitmire, C. J., Stanley, G. B., & Schwarz, C. (2015). Support for the slip hypothesis from whisker-related tactile perception of rats in a noisy environment. *Frontiers in Integrative Neuroscience*, *9*(October), e53. https://doi.org/10.3389/fnint.2015.00053

Waiblinger, C., Whitmire, C. J., Sederberg, A., Stanley, G. B., & Schwarz, C. (2018). Primary Tactile Thalamus Spiking Reflects Cognitive Signals. *The Journal of*

*Neuroscience*, *38*(21), 4870–4885. https://doi.org/10.1523/JNEUROSCI.2403-17.2018

Wang, Q., Webber, R. M., & Stanley, G. B. (2010). Thalamic synchrony and the adaptive gating of information flow to cortex. *Nature Neuroscience*, *13*(12), 1534–1541. https://doi.org/10.1038/nn.2670

Webber, R. M., & Stanley, G. B. (2004). Nonlinear Encoding of Tactile Patterns in the Barrel Cortex. *Journal of Neurophysiology*, *91*(5), 2010–2022. https://doi.org/10.1152/jn.00906.2003

Webber, R. M., & Stanley, G. B. (2006). Transient and Steady-State Dynamics of Cortical Adaptation. *Journal of Neurophysiology*, *95*(5), 2923–2932. https://doi.org/10.1152/jn.01188.2005

Whitmire, C. J., & Stanley, G. B. (2016). Rapid Sensory Adaptation Redux: A Circuit Perspective. *Neuron*, *92*(2), 298–315. https://doi.org/10.1016/j.neuron.2016.09.046

Whitmire, C. J., Waiblinger, C., Schwarz, C., & Stanley, G. B. (2016). Information Coding through Adaptive Gating of Synchronized Thalamic Bursting. *Cell Reports*, *14*(4), 795–807. https://doi.org/10.1016/j.celrep.2015.12.068

Wilent, W. B., & Contreras, D. (2005). Dynamics of excitation and inhibition underlying stimulus selectivity in rat somatosensory cortex. *Nature Neuroscience*, *8*(10), 1364–1370. https://doi.org/10.1038/nn1545

Wolfe, J., Hill, D. N., Pahlavan, S., Drew, P. J., Kleinfeld, D., & Feldman, D. E. (2008). Texture coding in the rat whisker system: Slip-stick versus differential resonance. *PLoS Biology*, *6*(8), 1661–1677. https://doi.org/10.1371/journal.pbio.0060215

Wright, N. C., Hoseini, M. S., & Wessel, R. (2017). Adaptation modulates correlated subthreshold response variability in visual cortex. *Journal of Neurophysiology*, *118*(2), 1257–1269. https://doi.org/10.1152/jn.00124.2017

Wright, N. C., Hoseini, M. S., Yasar, T. B., & Wessel, R. (2017). Coupling of synaptic inputs to local cortical activity differs among neurons and adapts after stimulus onset. *Journal of Neurophysiology*, *118*(6), 3345–3359. https://doi.org/10.1152/jn.00398.2017

Yu, J., Gutnisky, D. A., Hires, S. A., & Svoboda, K. (2016). Layer 4 fast-spiking interneurons filter thalamocortical signals during active somatosensation. *Nature Neuroscience*, *19*(12), 1647–1657. https://doi.org/10.1038/nn.4412

Yu, J., Hu, H., Agmon, A., & Svoboda, K. (2019). Recruitment of GABAergic Interneurons in the Barrel Cortex during Active Tactile Behavior. *Neuron*, *104*(2), 412-427.e4. https://doi.org/10.1016/j.neuron.2019.07.027

Zheng, H. J. V., Wang, Q., & Stanley, G. B. (2015). Adaptive shaping of cortical response selectivity in the vibrissa pathway. *Journal of Neurophysiology*, *113*(10), 3850–3865. https://doi.org/10.1152/jn.00978.2014

Zuo, Y., Safaai, H., Notaro, G., Mazzoni, A., Panzeri, S., & Diamond, M. E. (2015).

Complementary Contributions of Spike Timing and Spike Rate to Perceptual Decisions in Rat S1 and S2 Cortex. *Current Biology*, *25*(3), 357–363. https://doi.org/10.1016/j.cub.2014.11.065

## *Figure Captions*

**Figure 1. S1 exhibits sensory adaptation during wakefulness, and regular-spiking neurons are more profoundly adapted than fast-spiking neurons. A**. Experimental setup. We recorded in S1 of the awake, head-fixed mouse while presenting precise single-whisker stimulation. "Sawtooth" punctate whisker deflections were delivered either in isolation (control condition) or embedded in sensory white noise (adapted condition). **B**. Top: Grand mean +/- SEM waveforms for all well-isolated fast-spiking (FS, blue, N = 95) and regular-spiking (RS, red, N = 119) significantly responsive single-units recorded in S1 of awake mice (see Methods). Bottom: distribution of mean waveform widths (time from trough to subsequent peak) for all units, with color denoting RS and FS designation. **C**. Summed spiking activity of regular-spiking (RS, putative excitatory) and fast-spiking (FS, putative inhibitory) from one example recording session. Each row indicates spike times of all simultaneously-recorded RS (red) and FS (blue) neurons on a single trial. **D.** Grand-average mean (+/- SEM) rates for spontaneous activity (i.e., no sensory stimulation) and during the presentation of sensory white noise (with *** indicating $p < 0.001$, Wilcoxon signed-rank test). RS: spontaneous rate = 6.0 +/- 0.59 Hz, white-noise-evoked rate = 8.11 +/- 0.74 Hz, mean +/- SEM, 35.1% increase, $p = 6.17 \times 10^{-8}$, Wilcoxon signed-rank test, N = 119 units from 19 recording sessions, FS: spontaneous rate = 12.28 +/- 1.22 Hz, white-noise-evoked rate = 26.1 +/- 2.73 Hz, mean +/- SEM, 112.6% increase, $p = 2.41 \times 10^{-16}$, Wilcoxon signed-rank test, N = 95 units from 19 sessions. **E.** Grand PSTHs for all responsive RS (top, N = 119) and FS (bottom, N = 95) units, for two punctate stimulus velocities. **F.** Across-neuron mean (+/- SEM) firing rates for all responsive neurons, for 300 deg/s (left) and 900 deg/s (right) punctate stimuli (*: $0.01 \leq p < 0.05$; ***: $p < 0.001$, Wilcoxon singed-rank test). RS 300 deg/s mean +/- SEM control: 17.08 +/- 1.02, adapted: 11.36 +/- 1.01, 33.5% decrease, $p = 1.03 \times 10^{-15}$, Wilcoxon signed-rank test, N = 119 units from 19 recording sessions; 900 deg/s control: 17.19 +/- 1.25 Hz,

adapted: 9.92 +/- 1.08 Hz, 42.3% decrease, $p = 1.47 \times 10^{-8}$, N = 49 units from 8 sessions; FS: 300 deg/s control: 41.72 +/- 3.85 Hz, adapted: 34.1 +/- 3.39 Hz, 18.3% decrease $p = 2.90 \times 10^{-8}$, N = 95 units from 19 sessions; 900 deg/s control: 42.88 +/- 5.61 Hz, adapted: 40.03 +/- 6.43 Hz, 6.6% decrease p = 0.19, N = 29 units from 8 sessions. **G.** Population median (+/- SEM) normalized adapted responses for all responsive RS (red) and FS (blue) neurons (see Methods; ***: $p < 0.001$, Kruskal-Wallis test). RS 300 deg/s median normed adapted response = 0.61, FS median normed adapted response = 0.77, $p = 3.85 \times 10^{-5}$, Kruskal-Wallis test; 900 deg/s RS median normed adapted response = 0.47, FS median normed adapted response = 0.87, $p = 1.13 \times 10^{-4}$. **H.** Population median normalized adapted responses (+/- SEM) by binned cortical depth (see Methods).

**Figure 2. Adaptation reduces the theoretical detectability of punctate sensory stimuli. A.** Baseline and feature-evoked population spike rate distributions for one example RS unit (see Methods). For this unit (qualitatively representative of the average), adaptation decreased the mean population response rate, increasing the overlap of the baseline and feature-evoked distributions (right). **B.** Receiver operator characteristic (ROC) curves for example unit in (B), for the control (black line) and adapted (gray line) conditions, and associated area under ROC curve (AUROC) values. **C.** Grand average mean (+/- SEM) theoretical detectability (AUROC) vs. stimulus condition for all significantly responsive RS units (***: $p < 0.0005$, Wilcoxon signed-rank test). 300 deg/s control: mean +/- SEM AUROC = 0.81 +/- 0.02, adapted: 0.66 +/- 0.02, hybrid: 0.66 +/- 0.02, $p = 8.68 \times 10^{-12}$ control vs. adapted, $p = 1.33 \times 10^{-16}$ control vs. hybrid, p = 0.77 adapted vs. hybrid, Wilcoxon signed-rank test, N = 119 units from 19 recording sessions; 900 deg/s control: 0.89 +/- 0.02, adapted: 0.73 +/- 0.03, hybrid: 0.71 +/- 0.03, $p = 4.37 \times 10^{-6}$ control vs. adapted, $p = 1.61 \times 10^{-7}$ control vs. hybrid, p = 0.23 adapted vs. hybrid, N = 49 units from 8 recording sessions.

**Figure 3. Adaptation increases response latency and reduces pairwise synchronous spiking in S1. A.** Calculation of response onset properties for example RS unit. Spike trains for each trial were convolved with a Gaussian kernel and summed

across trials, resulting in a convolved spike count ($\tilde{s}$), from which we calculated response onset times ($T_{onset}$) and max rate of change in $\tilde{s}$ immediately after $T_{onset}$ (max $d\tilde{s}/dt$, see Methods). **B.** Grand mean onset times for RS (red) and FS (blue) neurons, for control and adapted responses to 300 deg/s stimulus (***: $p < 0.001$; single gray bar: $p \geq 0.05$, Wilcoxon signed-rank test, control vs. adapted). 300 deg/s RS mean +/ SEM control: $T_{onset}$ = 8.81 +/- 0.53 ms, adapted: 15.31 +/- 0.98 ms, 73.9% increase, $p = 3.11 \times 10^{-11}$, Wilcoxon signed-rank test, N = 119 units; FS control: $T_{onset}$ = 6.69 +/- 0.37 ms, adapted: 8.95 +/- 0.7 ms, 33.9% increase, $p = 8.11 \times 10^{-7}$, N = 95 units; 900 deg/s RS control: $T_{onset}$ = 7.89 +/- 0.49 ms, adapted: 11.36 +/- 1.07 ms, 43.9% increase, $p = 1.70 \times 10^{-5}$, N = 49 units; FS control: $T_{onset}$ = 5.67 +/- 0.29 ms, adapted: 6.27 +/- 0.63 ms, p = 0.27. **C.** Illustration of synchronous spike-count calculation. The grand cross-correlogram (CCG) was constructed using all valid pairs of simultaneously-recorded S1 units, then scaled by the number of contributing pairs, and shuffle-corrected (see Methods). The synchronous spike count was the number of spikes in a +/- 7.5 ms window around zero lag. **D.** Grand RS-RS CCGs for responses to 300 deg/s stimulus, for the control (dark red) and adapted (light red) conditions. Bands indicate 99.9% confidence intervals (from re-sampling spikes with replacement, see Methods). **E.** Synchronous AP counts for control and adapted responses, calculated from RS-RS grand CCGs in (D). Error bars indicate 99.9% confidence intervals (from re-sampling spikes with replacement, see Methods). RS-RS pairs: 300 deg/s mean +/- 99.9% confidence interval control: synch AP count = 65.93 +/- 3.31 spikes/pair, adapted: 22.14 +/- 2.11 spikes/pair, 66.4% decrease, $p < 0.001$, N = 189 valid pairs from 17 sessions; 900 deg/s control: 135.64 +/- 7.53 spikes/pair; adapted: 25.67 +/- 3.65 spikes/pair, 81.1% decrease, $p < 0.001$, N = 55 valid pairs from 6 sessions. **F** and **G.** Same as (D) and (E), but for valid FS-FS pairs. FS-FS pairs: 300 deg/s control: 253.47 +/- 8.64 spikes/pair, adapted: 173.73 +/- 7.56 spikes/pair, 31.5% decrease, $p < 0.001$, N = 118 valid pairs from 17 sessions; 900 deg/s control: 597.33 +/- 23.79 spikes/pair; adapted: 379.8 +/- 19.6 spikes/pair, 36.4% decrease, $p < 0.001$, N = 33 valid pairs from 6 sessions, see Methods for definition of “valid pairs”.

1413 **Figure 4. S1 sensory responses are also adapted under anesthesia, but RS cells**
1414 **are not differentially adapted. A.** Experimental setup. S1 sensory responses were
1415 recorded in mice lightly-anesthetized with isoflurane (see Methods). **B.** Summed spiking
1416 activity of regular-spiking (RS, putative excitatory) and fast-spiking (FS, putative
1417 inhibitory) from one example recording session. Each row indicates spike times of all
1418 simultaneously-recorded RS (red) and FS (blue) neurons on a single trial. **C.** Grand-
1419 average mean (+/- SEM) rates for spontaneous activity (i.e., no sensory stimulation) and
1420 during the presentation of sensory white noise (with *** indicating $p < 0.001$, Wilcoxon
1421 signed-rank test). RS: spontaneous rate = 2.31 +/- 0.37 Hz, white-noise-evoked rate =
1422 3.77 +/- 0.4 Hz, mean +/- SEM, 63.4% increase, $p = 2.44 \times 10^{-7}$, Wilcoxon signed-rank
1423 test, N = 46 units from 14 sessions, Fig. 2C; FS: spontaneous rate = 0.83 +/- 0.26 Hz,
1424 white-noise-evoked rate = 6.29 +/- 0.92 Hz, mean +/- SEM, 657% increase, $p = 5.60 \times$
1425 $10^{-5}$, N = 21 units from 14 sessions. **D.** Sensory response grand PSTHs for all responsive
1426 RS (left, N = 46) and FS (right, N = 21) units recorded under anesthesia, for 300 deg/s
1427 punctate stimulus velocity. **E.** Grand mean (+/- SEM) rates for cells contributing to PSTHs
1428 in (D). RS mean +/- SEM control: 12.27 +/- 0.88 Hz, adapted: 7.75 +/- 1.01, 36.8%
1429 decrease, $p = 9.82 \times 10^{-5}$; FS control: 18.61 +/- 2.19 Hz, adapted: 11.94 +/- 2.61, 35.8%
1430 decrease, $p = 0.001$. **F.** Population median (+/- SEM) normalized adapted responses
1431 for all responsive RS (red) and FS (blue) neurons (see Methods). RS 300 deg/s median
1432 normed adapted response = 0.54, FS median normed adapted response = 0.57, $p = 0.91$,
1433 Kruskal-Wallis test.

1434

1435 **Figure 5. Adaptation reduces tonic and burst firing rates, and synchronous spike**
1436 **counts, in VPm sensory responses. A.** Experimental setup. We recorded extracellular
1437 spiking in VPm of the awake mouse, primarily using high-density silicon probes (see
1438 Methods). **B.** Top: summed spiking activity of all well-isolated, responsive, putative VPm
1439 units (see Methods) from one example recording session. Each row indicates spike times
1440 of all such simultaneously-recorded units on a single trial. **C.** Grand-average mean (+/-
1441 SEM) rates for spontaneous activity (i.e., no sensory stimulation) and during the
1442 presentation of sensory white noise (with *** indicating $p < 0.001$, Wilcoxon signed-rank

1443 test). Mean +/- SEM spontaneous: rate = 10.5 +/- 1.29 Hz, white noise: rate = 15.58 +/-
1444 2.5 Hz, 48.4% increase $p = 9.63 \times 10^{-4}$, Wilcoxon signed-rank test, N = 30 units from 9
1445 recording sessions. **D.** Criteria for classification of putative tonic (black) and burst (red)
1446 VPm spikes. **E.** Grand PSTHs for tonic (black) and burst (red) spikes from all putative
1447 VPm neurons, for 300 deg/s punctate stimulus. Note the presence of both a short-latency
1448 primary peak, and a shorter, secondary peak in tonic firing rates (Fig. 5E). This secondary
1449 peak in the grand PSTH resulted from a subset of neurons with both early and late
1450 responses – often within individual trials – and was likely evoked by the return of the
1451 whisker to resting position in the second half of the sawtooth waveform. **F.** Across-
1452 neuron mean (+/- SEM) firing rates for all putative VPm neurons (**: $0.001 \leq p < 0.01$; ***:
1453 $p < 0.001$, Wilcoxon singed-rank test). Tonic 300 deg/s mean +/- SEM rate control: 30.2
1454 +/- 3.41 Hz, adapted: 24.32 +/- 2.92 Hz, 19.5% decrease, N = 30 units, p = 0.002,
1455 Wilcoxon signed-rank test; 900 control: 29.98 +/- 3.47 Hz, adapted: 26.87 +/- 3.18 Hz, N
1456 = 16 units, p = 0.22; burst: 300 deg/s control: 3.79 +/- 1.08, adapted: 1.37 +/- 0.73 Hz,
1457 64.0% decrease, $p = 6.21 \times 10^{-4}$; 900 deg/s control: 5.75 +/- 3.13 Hz, adapted: 2.02 +/-
1458 0.88, 64.9% decrease, $p = 4.6 \times 10^{-3}$. **G.** Grand shuffle-corrected cross-correlograms for
1459 all simultaneously-recorded putative VPm neurons, for the control (black) and adapted
1460 (gray) conditions. Bands indicate 99.9% confidence intervals (from re-sampling spikes
1461 with replacement, see Methods). **H.** Mean synchronous AP counts, calculated from
1462 CCGs in (G), with error bars indicating 99.99% confidence intervals (***: $p < 0.001$, re-
1463 sampling spikes with replacement). 300 deg/s mean +/- 99.9% confidence interval
1464 control: synch AP count = 42.96 +/- 8.9 spikes/pair, adapted: 16.6 +/- 6.19 spikes/pair,
1465 61.4% decrease, $p < 0.001$, N = 48 valid pairs from 7 sessions; 900 deg/s control: 54.1
1466 +/- 10.43 spikes/pair; adapted: 31.51 +/- 9.24 spikes/pair, 41.7% decrease, $p < 0.001$, N
1467 = 37 valid pairs from 3 sessions, see Methods for definition of "valid pairs"

1468

1469 **Figure 6. Optogenetic elevation of baseline VPm firing rate does not adapt S1**
1470 **sensory responses. A.** Experimental setup. We recorded extracellular spiking activity
1471 from topographically-aligned VPm barreloids and S1 barrels in awake, head-fixed,
1472 transgenic mice expressing Channelrhodopsin in VPm/VPl neurons (see Methods). **B.**

1473 Summed spiking activity of all well-isolated, responsive putative VPm (top) and S1
1474 (bottom) units from one example recording session. Each row indicates spike times of all
1475 such simultaneously-recorded units in that brain region on a single trial. **C.** Grand mean
1476 (+/- SEM) firing rates for spontaneous activity ("spont"), and during presentation of the
1477 adapting sensory stimulus ("white noise") and optogenetic depolarization of VPm ("LED"),
1478 for VPm (top) and S1 (bottom; *: $0.005 \leq p < 0.025$; **: $5 \times 10^{-4} \leq p < 5 \times 10^{-3}$; ***: $p < 5 \times$
1479 $10^{-4}$). VPm mean +/- SEM rate spontaneous: 7.68 +/- 1.1 Hz, white noise: 11.05 +/- 1.99
1480 Hz, LED: 14.27 +/- 2.81 Hz, 44.0% increase spont vs. white noise, $p = 0.011$, Wilcoxon
1481 signed-rank test, 85.9% increase spont vs. LED, $p = 0.011$, 29.2% increase white noise
1482 vs. LED, $p = 0.91$, N = 20 units from six sessions; S1 spontaneous: 8.87 +/- 0.82 Hz,
1483 white noise: 16.32 +/- 2.05 Hz, LED: 10.03 +/- 1.05 Hz, 87.7% increase spont vs. white
1484 noise, $p = 5.05 \times 10^{-10}$, 15.3% increase spont vs. LED, $p = 0.11$, spont vs. LED, 38.6%
1485 decrease white noise vs. LED, $p = 8.42 \times 10^{-5}$, N = 88 units from six sessions. **D.** Left:
1486 grand PSTHs for each stimulus condition, for VPm (top) and S1 (bottom). Right: Grand
1487 mean (+/- SEM) firing rates for each condition. Asterisks as in (C). S1 mean +/- SEM
1488 rate control: 27.33 +/- 2.61 Hz, adapted: 20.91 +/- 2.47 Hz, LED: 27.82 +/- 2.79 Hz, 23.5%
1489 decrease control vs. adapted, $p = 1.39 \times 10^{-9}$, 1.76% increase control vs. LED, $p = 0.89$,
1490 Wilcoxon signed-rank test; VPm control: 29.12 +/- 4.82 Hz, adapted: 19.07 +/- 3.1 Hz,
1491 LED: 36.44 +/- 5.35 Hz, 34.5% decrease control vs. adapted, $p = 0.003$, 25.16% increase
1492 control vs. LED, $p = 0.06$. **E.** Top: Grand VPm CCGs for each stimulus condition. Bands
1493 indicate 99.9% confidence intervals (re-sampling spikes with replacement (see Methods).
1494 Bottom: synchronous spike counts calculated from CCGs in (E, Top), for each stimulus
1495 condition. Error bars indicate 99.9% confidence intervals (re-sampling spikes with
1496 replacement (see Methods). Mean +/- 99.9% confidence interval synch AP count control:
1497 47.14 +/- 11.0 spikes/pair, LED: 51.83 +/- 12.94 spikes/pair, adapted: 20.08 +/- 8.53
1498 spikes/pair, $p \geq 0.05$ control vs. LED, $p < 0.001$ control vs. adapted, re-sampling spikes
1499 with replacement, N = 36 pairs from 19 units in five sessions.

1500

1501 **Figure 7. S1 responses to direct optogenetic stimulation of TC terminals are not**
1502 **adapted by sensory white noise. A.** Experimental setup for extracellular recordings.

1503 S1 spiking activity was recorded in mice lightly-anesthetized with isoflurane (see
1504 Methods). These transgenic mice expressed Channelrhodopsin in VPm cell bodies,
1505 axons, and thalamocortical (TC) axon terminals. An optic fiber positioned above the
1506 cortical surface was used to deliver punctate optogenetic stimulation to TC terminals on
1507 "light feature" stimulation trials (see Methods). **B.** Grand PSTHs (using all sensory-
1508 responsive single- and multi-units, see Methods) for sensory feature (black, left) and light
1509 feature (blue, right) trials, for control (empty histogram) and adapted (filled histogram)
1510 conditions. **C.** Across-unit mean (+/- SEM) punctate-stimulus-evoked firing rates vs
1511 stimulus condition for all responsive single- and multi-units, for sensory feature (black,
1512 left) and light feature (blue, right) stimuli. (***: $p < 0.001$, Wilcoxon singed-rank test).
1513 Sensory feature mean +/- SEM control: 18.38 +/- 1.27 Hz, adapted: 6.59 +/- 0.65 Hz,
1514 64.17% decrease, $p = 1.39 \times 10^{-12}$ N = 71 units, Wilcoxon signed-rank test. Light feature
1515 mean +/- SEM control: 11.7 +/- 0.95 Hz, adapted: 11.38 +/- 0.99 Hz, 2.75% decrease, p
1516 = 0.19. **D.** Distributions of normalized adapted responses for all valid units (see
1517 Methods). Triangles at top denote population median values (***: $p < 0.001$, Wilcoxon
1518 signed-rank test). Population median normalized adapted response = -0.29 light feature
1519 trials, 0.96 sensory feature trials, $p = 3.12 \times 10^{-11}$, Wilcoxon signed-rank test. **E.** Left:
1520 experimental setup for in vivo S1 patch clamp recordings in lightly-anesthetized
1521 transgenic mice. Right: Across-trial median membrane potential responses to sensory
1522 features (black traces) and light features (blue traces), for one example S1 neuron. **F.**
1523 Properties of subthreshold responses to sensory features (left) and light features (right):
1524 subthreshold response amplitude (top), and time from stimulus onset to peak
1525 subthreshold response ($T_{peak}$, center) for each of the four recorded cells. Dark lines
1526 connecting pairs of data points indicate significant difference across stimulus conditions
1527 ($p < 0.05$, Wilcoxon signed-rank test), and light lines indicate non-significance.

1528

1529 **Figure 8. A thalamocortical network model identifies synchronous VPm spikes and**
1530 **feedforward inhibition as key mechanisms underlying response adaptation. A.**
1531 Model schematic (see Methods). **B.** Grand mean PSTHs for VPm spike times used to
1532 stimulate the network (top) and network excitatory and inhibitory neurons, for the control

(empty PSTHs) and adapted (filled PSTHs) conditions. **C.** Normalized adapted responses for both simulated stimulus velocities (see Methods). For each condition, the response is defined to be the peak of the grand PSTH, and the normalized adapted response is the adapted value divided by the unadapted value. Error bars indicate 95% confidence intervals from re-sampling neurons with replacement. **D.** Grand exc-exc (left) and inh-inh (right) CCGs for 200 randomly-selected pairs of network neurons, for the control (dark line) and adapted (lighter line) conditions. CCGs normalized to max value in control condition for visualization purposes. **E.** Top: grand CCGs for VPm inputs to model in the control (dark line) and adapted (lighter line) conditions (corresponding to PSTHs in B, top). Bottom: grand CCGs for VPm inputs in the control (dark line) and "reduced synch" (lighter line) conditions, where the "reduced synch" condition results from manual changes to drawn VPm spike times (see Methods). **F.** Same as in B, but for control and "reduced synch" simulations. **G.** Normalized "reduced synch" response for simulations in (F). **H.** Same as in (D), but for simulations in (F). **I.** Model schematic for "identical TC connectivity" network (see Results and Methods). **J.** Grand excitatory (top) and inhibitory (bottom) PSTHs for "identical TC connectivity" network. **K, L.** Same as in (G, H), but for "identical TC connectivity" network.

# Figure 1

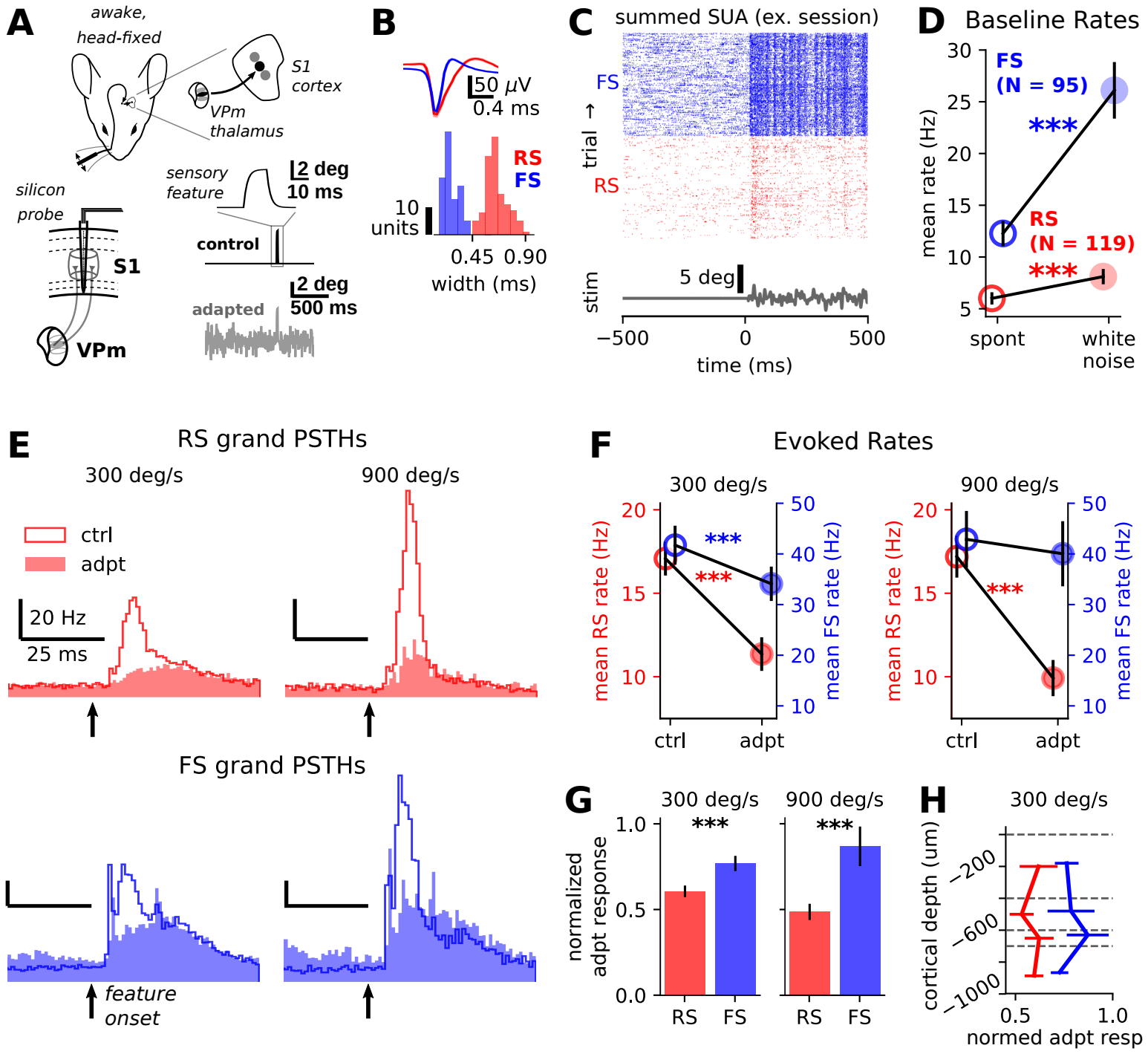
A
awake,
head-fixed
S1
cortex
VPm
thalamus
silicon
probe
S1
VPm
sensory
feature
2 deg
10 ms
control
2 deg
500 ms
adapted
B
50 μV
0.4 ms
RS
FS
10
units
0.45 0.90
width (ms)
C
summed SUA (ex. session)
FS
trial →
RS
stim
5 deg
−500
0
500
time (ms)
D
Baseline Rates
FS
(N = 95)
***
RS
(N = 119)
***
mean rate (Hz)
spont
white
noise
E
RS grand PSTHs
300 deg/s
900 deg/s
ctrl
adpt
20 Hz
25 ms
FS grand PSTHs
feature
onset
F
Evoked Rates
300 deg/s
900 deg/s
mean RS rate (Hz)
mean FS rate (Hz)
***
ctrl
adpt
G
300 deg/s
900 deg/s
normalized
adpt response
***
RS
FS
H
300 deg/s
cortical depth (um)
normed adpt resp

**Figure 2**

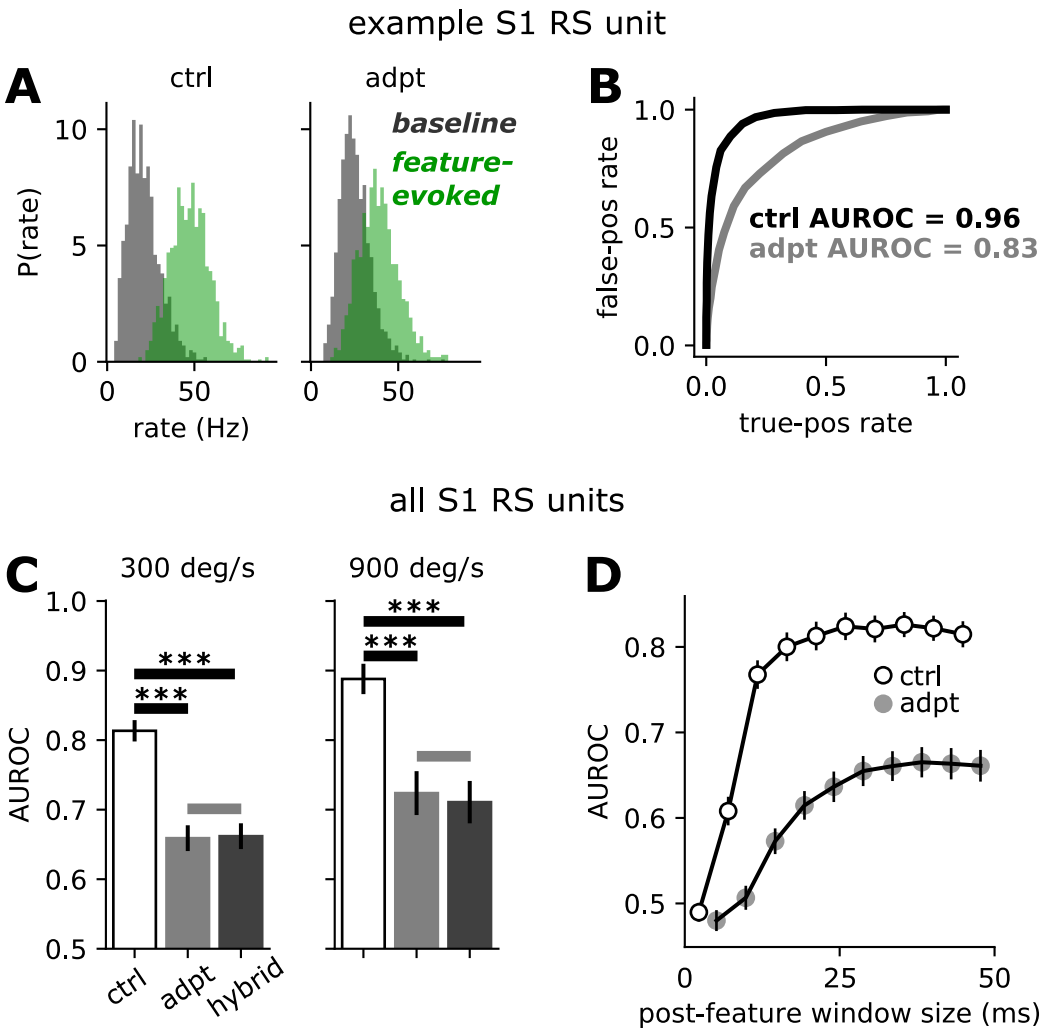
example S1 RS unit
A
ctrl
adpt
baseline
feature-evoked
P(rate)
rate (Hz)
B
false-pos rate
true-pos rate
ctrl AUROC = 0.96
adpt AUROC = 0.83
all S1 RS units
C
300 deg/s
900 deg/s
AUROC
ctrl
adpt
hybrid
***
D
AUROC
ctrl
adpt
post-feature window size (ms)

# Figure 3

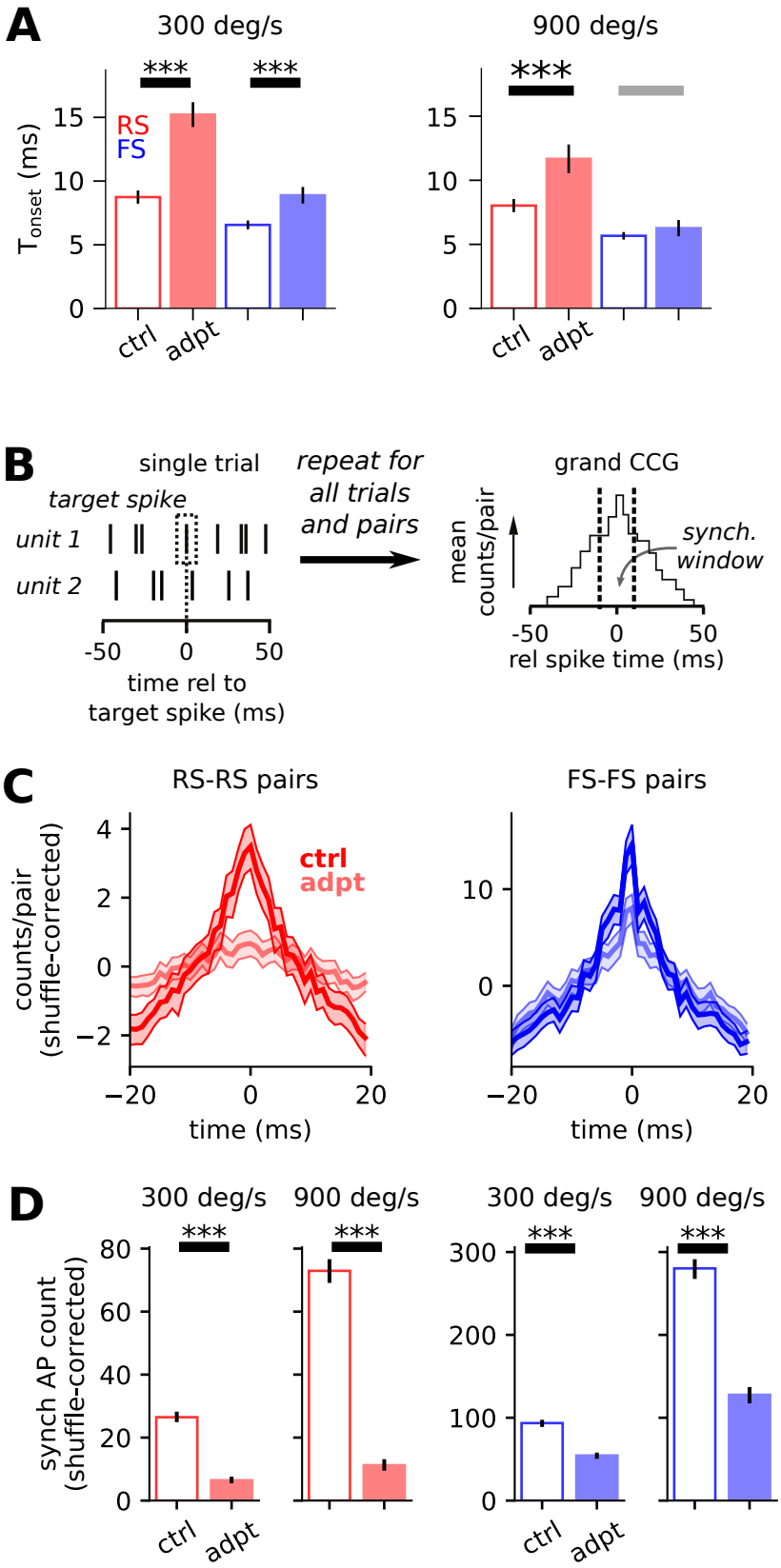
A
300 deg/s
900 deg/s
***
***
***
RS
FS
$T_{onset}$ (ms)
15
10
5
0
ctrl
adpt
B
single trial
target spike
unit 1
unit 2
-50
0
50
time rel to
target spike (ms)
repeat for
all trials
and pairs
grand CCG
mean
counts/pair
synch.
window
-50
0
50
rel spike time (ms)
C
RS-RS pairs
FS-FS pairs
ctrl
adpt
counts/pair
(shuffle-corrected)
4
2
0
−2
10
0
−20
0
20
time (ms)
D
300 deg/s
900 deg/s
300 deg/s
900 deg/s
***
synch AP count
(shuffle-corrected)
80
60
40
20
0
300
200
100
0
ctrl
adpt

# Figure 4

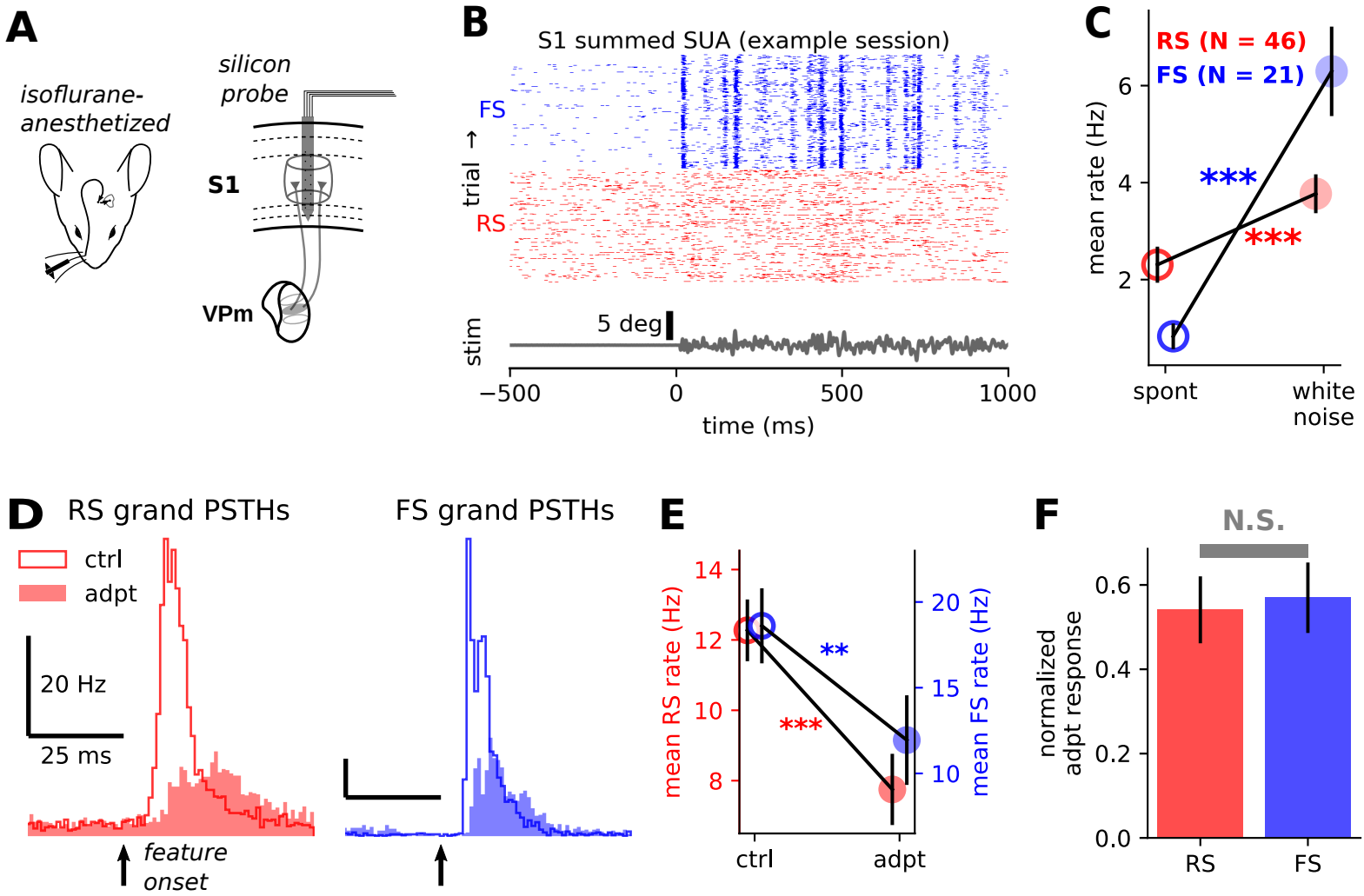
A
isoflurane-
anesthetized
silicon
probe
S1
VPm
B
S1 summed SUA (example session)
FS
trial →
RS
stim
5 deg
−500
0
500
1000
time (ms)
C
RS (N = 46)
FS (N = 21)
mean rate (Hz)
6
4
2
***
***
spont
white
noise
D
RS grand PSTHs
FS grand PSTHs
ctrl
adpt
20 Hz
25 ms
feature
onset
E
mean RS rate (Hz)
14
12
10
8
mean FS rate (Hz)
20
15
10
**
***
ctrl
adpt
F
N.S.
normalized
adpt response
0.6
0.4
0.2
0.0
RS
FS

# Figure 5

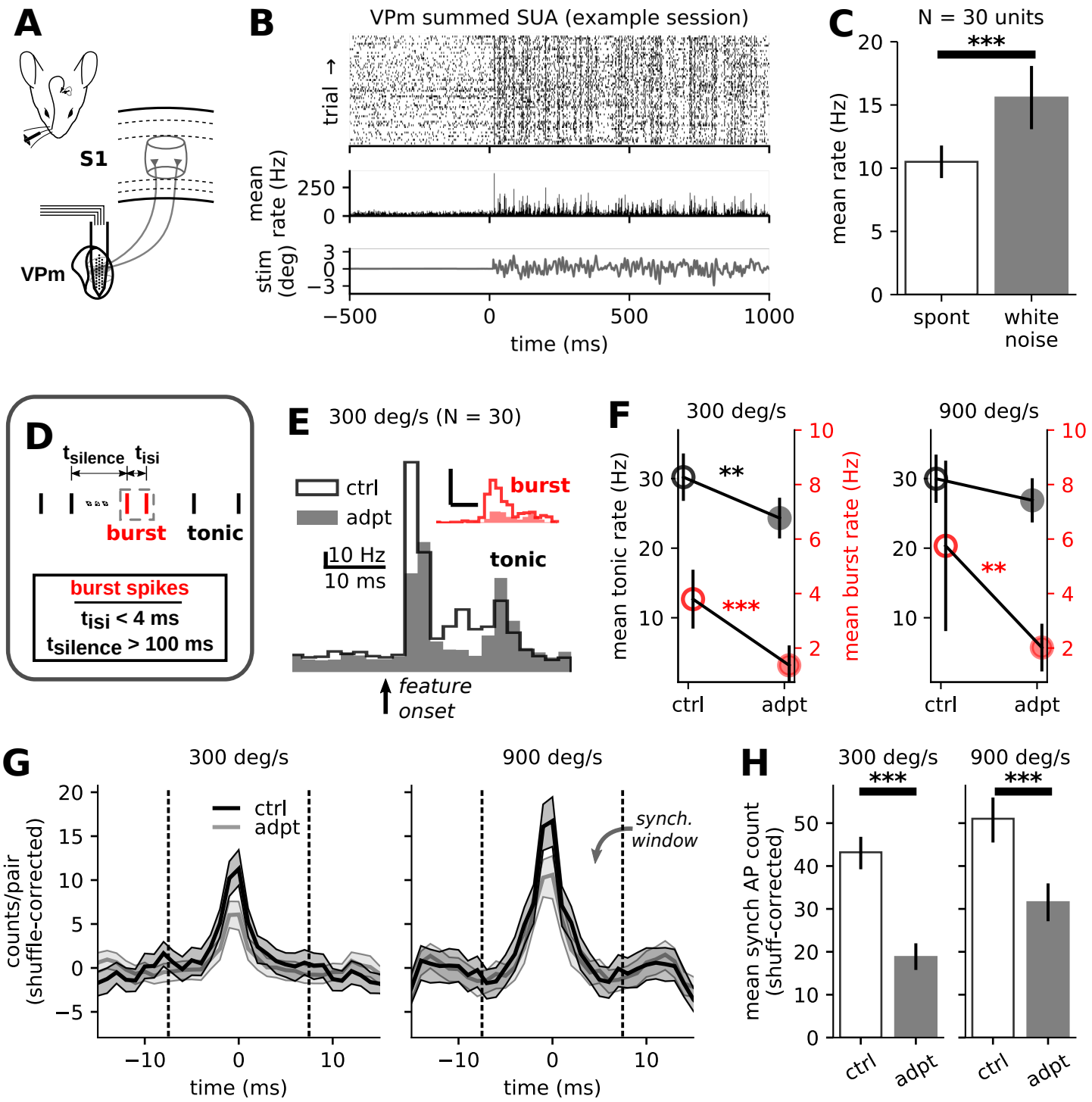
A
S1
VPm
B
VPm summed SUA (example session)
trial →
mean rate (Hz)
250
0
stim (deg)
3
0
−3
−500
0
500
1000
time (ms)
C
N = 30 units
***
mean rate (Hz)
20
15
10
5
0
spont
white noise
D
$t_{silence}$ $t_{isi}$
burst
tonic
burst spikes
$t_{isi}$ < 4 ms
$t_{silence}$ > 100 ms
E
300 deg/s (N = 30)
ctrl
adpt
burst
10 Hz
10 ms
tonic
feature onset
F
300 deg/s
900 deg/s
mean tonic rate (Hz)
mean burst rate (Hz)
**
***
**
ctrl
adpt
G
300 deg/s
900 deg/s
ctrl
adpt
synch. window
counts/pair (shuffle-corrected)
20
15
10
5
0
−5
−10
0
10
time (ms)
H
300 deg/s
900 deg/s
***
***
mean synch AP count (shuff-corrected)
50
40
30
20
10
0
ctrl
adpt
ctrl
adpt

# Figure 6

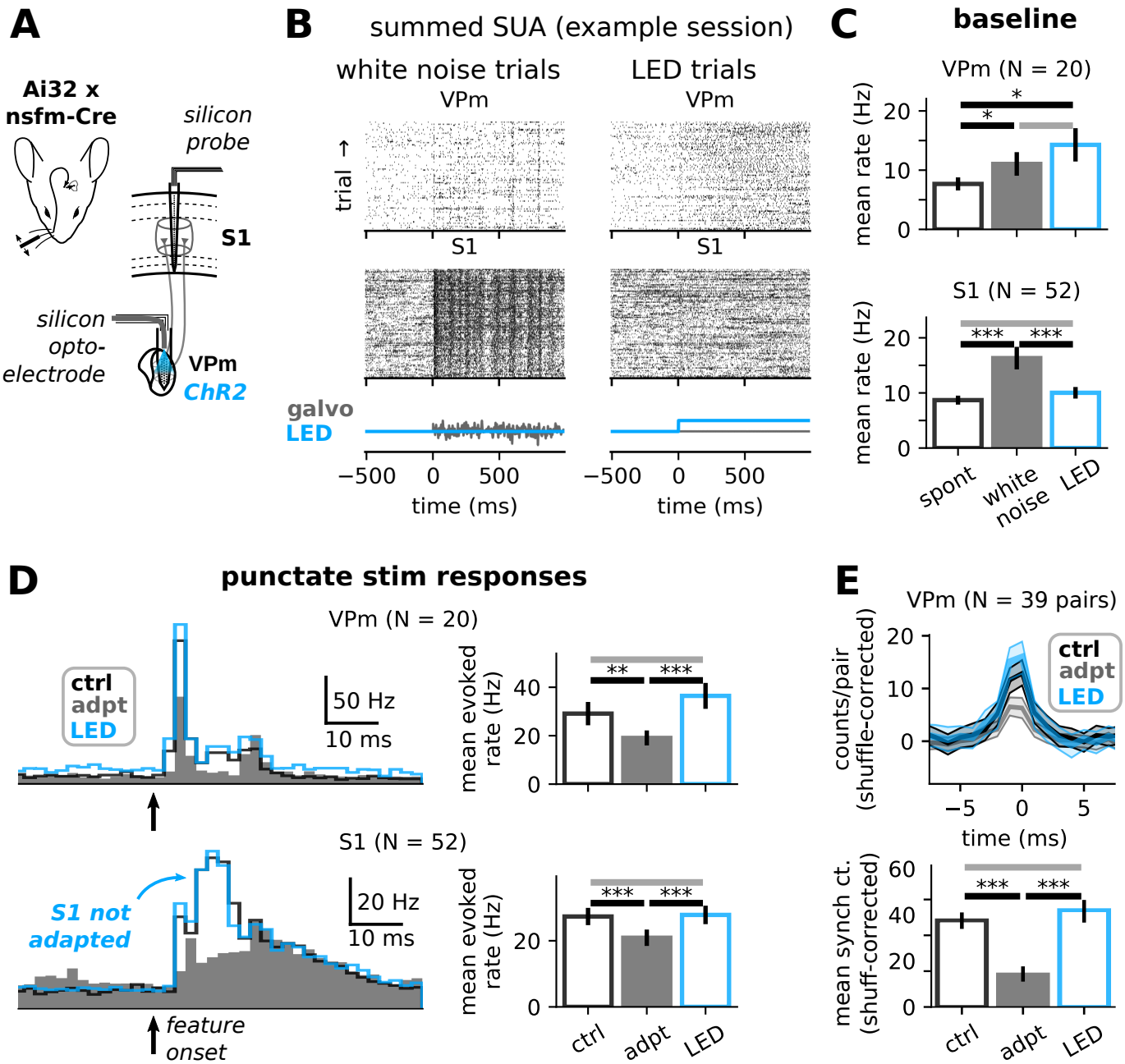
A
Ai32 x
nsfm-Cre
silicon
probe
S1
silicon
opto-
electrode
VPm
ChR2
B
summed SUA (example session)
white noise trials
LED trials
VPm
VPm
trial →
S1
S1
galvo
LED
−500
0
500
time (ms)
−500
0
500
time (ms)
C
baseline
VPm (N = 20)
mean rate (Hz)
S1 (N = 52)
mean rate (Hz)
spont
white
noise
LED
D
punctate stim responses
VPm (N = 20)
ctrl
adpt
LED
50 Hz
10 ms
mean evoked
rate (Hz)
S1 (N = 52)
S1 not
adapted
20 Hz
10 ms
feature
onset
mean evoked
rate (Hz)
ctrl
adpt
LED
E
VPm (N = 39 pairs)
counts/pair
(shuffle-corrected)
ctrl
adpt
LED
time (ms)
mean synch ct.
(shuff-corrected)
ctrl
adpt
LED

# Figure 7

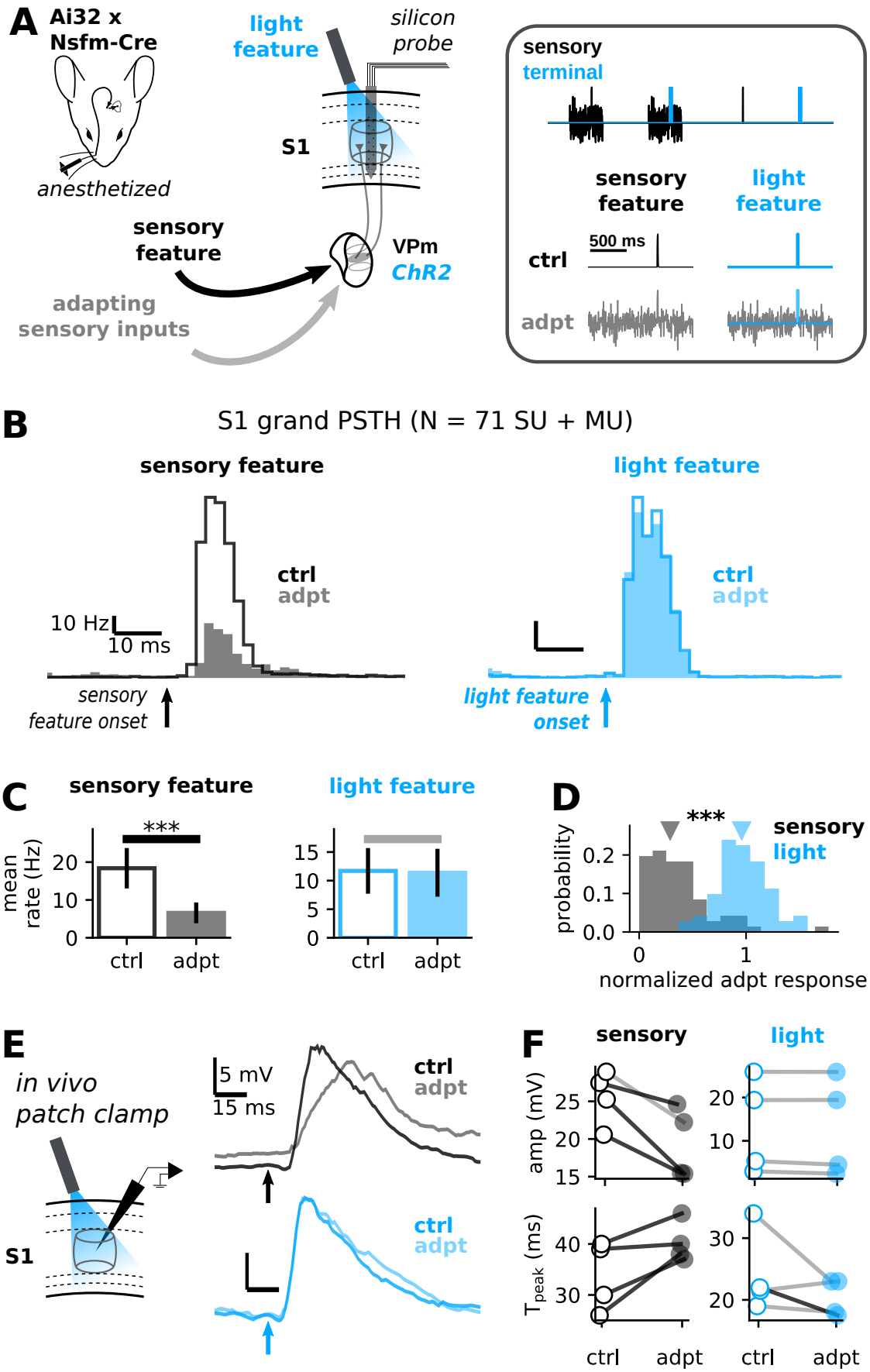
A
Ai32 x
Nsfm-Cre
anesthetized
light
feature
silicon
probe
S1
sensory
feature
VPm
ChR2
adapting
sensory inputs
sensory
terminal
sensory
feature
light
feature
500 ms
ctrl
adpt
B
S1 grand PSTH (N = 71 SU + MU)
sensory feature
light feature
ctrl
adpt
10 Hz
10 ms
sensory
feature onset
light feature
onset
C
sensory feature
light feature
mean
rate (Hz)
***
ctrl
adpt
D
probability
***
sensory
light
normalized adpt response
E
in vivo
patch clamp
S1
5 mV
15 ms
ctrl
adpt
F
sensory
light
amp (mV)
$T_{peak}$ (ms)
ctrl
adpt

**Figure 8**

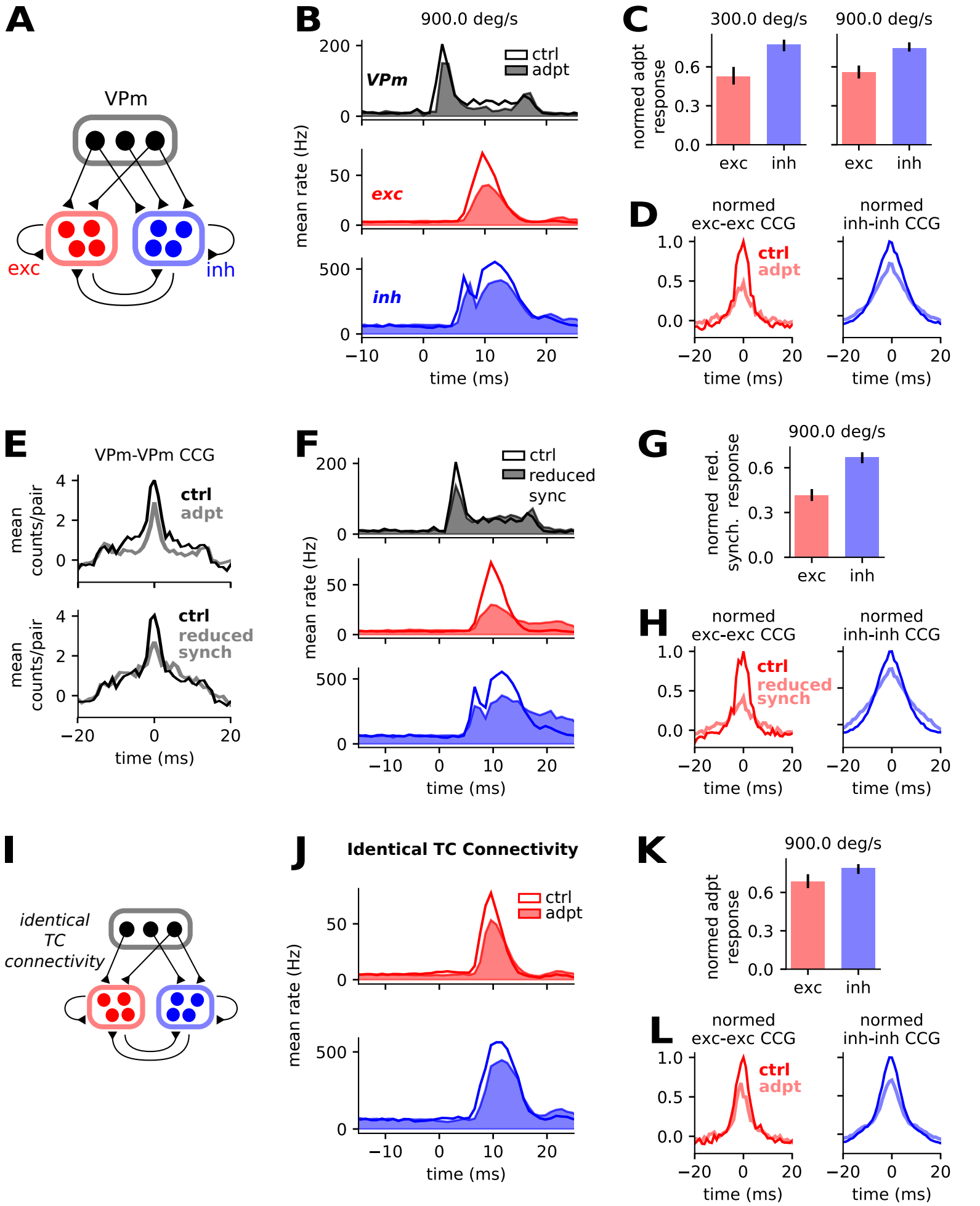
A
VPm
exc
inh
B
900.0 deg/s
ctrl
adpt
VPm
exc
inh
mean rate (Hz)
time (ms)
C
300.0 deg/s
900.0 deg/s
normed adpt response
exc
inh
D
normed exc-exc CCG
normed inh-inh CCG
ctrl
adpt
time (ms)
E
VPm-VPm CCG
mean counts/pair
ctrl
adpt
ctrl
reduced synch
time (ms)
F
ctrl
reduced sync
mean rate (Hz)
time (ms)
G
900.0 deg/s
normed red. synch. response
exc
inh
H
normed exc-exc CCG
normed inh-inh CCG
ctrl
reduced synch
time (ms)
I
identical TC connectivity
J
Identical TC Connectivity
ctrl
adpt
mean rate (Hz)
time (ms)
K
900.0 deg/s
normed adpt response
exc
inh
L
normed exc-exc CCG
normed inh-inh CCG
ctrl
adpt
time (ms)